

Accessing Realistic Models for the $\text{WO}_3\text{-SiO}_2$ Industrial Catalyst through the Design of Organometallic Precursors

Y. Bouhouste,[†] D. Grekov,[‡] K. C. Szeto,[†] N. Merle,[†] A. De Mallmann,[†] F. Lefebvre,[†] G. Raffa,[†] I. Del Rosal,[§] L. Maron,^{*,§} R. M. Gauvin,[‡] L. Delevoye,^{*,‡} and M. Taoufik^{*,†}

[†]Laboratoire de Chimie, Catalyse, Polymères et Procédés, UMR 5265 CNRS/ESCP-E-Lyon/UCBL, ESCPE Lyon, F-308, 43 Boulevard du 11 Novembre 1918, F-69616 Villeurbanne Cedex, France

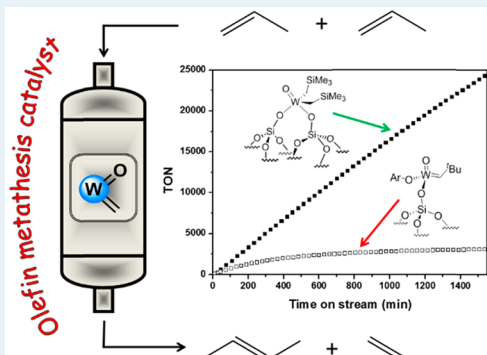
[‡]Univ. Lille, CNRS, Centrale Lille, ENSCL, Univ. Artois, UMR 8181 - UCCS - Unité de Catalyse et Chimie du Solide, F-59000 Lille, France

[§]Laboratoire de Physico-Chimie des Nano-Objets, CNRS UMR 5215, Université de Toulouse, INSA, UPS, 135 avenue de Rangueil, F-31077 Toulouse, France

Supporting Information

ABSTRACT: In order to access realistic models to the industrial olefin metathesis catalyst $\text{WO}_3\text{/SiO}_2$, which is the bигrafted tungsten oxo alkylidene species $[(\equiv\text{SiO})_2\text{WO}(\text{=CHR})]$, we targeted the parent bis-alkyl oxo derivative $[(\equiv\text{SiO})_2\text{WOR}_2]$ prone to carbene formation. Thus, grafting of $[\text{WO}(\text{CH}_2\text{EMe}_3)_3\text{Cl}]$ ($\text{E} = \text{C}$, **1-Np**; $\text{E} = \text{Si}$, **1-Ns**) onto silica dehydroxylated at 200°C was performed. While **1-Np** affords the monopodal species $[(\equiv\text{SiO})\text{WO}(\text{CH}_2\text{CMe}_3)_3]$ (**2-Np**), the neosilyl derivative **1-Ns** reacts to yield the well-defined bipodal species $[(\equiv\text{SiO})_2\text{WO}(\text{CH}_2\text{SiMe}_3)_2]$ (**2-Ns**), via consecutive HCl and SiMe_4 release. This was demonstrated by mass balance analysis, elemental analysis, IR, advanced solid-state NMR (1D and 2D ^1H , ^{13}C , ^{29}Si , and ^{17}O), and EXAFS. Furthermore, DFT calculations allowed understanding and rationalizing the experimental results regarding grafting selectivity. The material **2-Ns** proved to lead to the most stable and efficient supported tungsten oxo catalyst for propene metathesis under dynamic conditions at 80°C .

KEYWORDS: tungsten, metathesis, surface chemistry, DFT calculations, solid-state NMR



INTRODUCTION

Catalytic conversion of hydrocarbons into valuable products is of strategic importance in today's world economy. Different technologies to upgrade hydrocarbons, such as synthesis gas production,¹ Fischer–Tropsch synthesis,² alkane dehydrogenation,³ methanol synthesis,⁴ methanol to gasoline,⁵ methanol to olefin,⁶ and olefin polymerization⁷ and metathesis,⁸ have already been established. Among the different transformations mentioned, olefin metathesis is a versatile reaction that is applied to a wide range of substrates extending from large-scale industrial processes to fine chemistry. Indeed, a most critical point is the catalyst performance in terms of activity, selectivity, and stability. Thus, the development of robust and preferably heterogeneous olefin metathesis catalysts is of high interest, since it would probably be adaptable to a large variety of important substrates and different reactor designs.

Typically heterogeneous olefin metathesis catalysts are based on supported Mo, Re, and W on oxides such as silica, alumina, and silica–alumina due to their highly oxophilic properties, giving a stable attachment between the metal and the oxide support. These elements have been extensively studied in academic and industrial laboratories, and certain systems have even been commercialized, mainly to convert gaseous olefins to

valuable products. The supported Mo and W oxides used as catalysts in gas-phase applications on a large scale in the Shell Higher Olefins Process (SHOP), Phillips' Neohexene process, and ABB Lummus' Olefins Conversion Technology (OCT), require elevated reaction temperatures. For example, the SHOP metathesis catalyst, $\text{MoO}_3/\gamma\text{-Al}_2\text{O}_3$, operates at $100\text{--}200^\circ\text{C}$, while the $\text{WO}_3\text{/SiO}_2$ catalyst used for OCT and the Neohexene process works around 400°C .^{9,10} $\text{WO}_3\text{/SiO}_2$ has become one of the most important catalytic systems due to its fairly low preparation cost and robustness. This catalyst is classically prepared by aqueous impregnation of ammonium metatungstate accompanied by calcination.¹¹ Although different preparation techniques for this catalyst have been investigated,^{12–17} the final calcination step leads inevitably to a mixture of different surface species that are difficult to distinguish. Despite the complexity of the surface chemistry of the rather simple $\text{WO}_3\text{/SiO}_2$ catalyst, the active site proposed a couple of decades ago consisting of a bipodal

Received: August 10, 2015

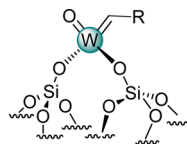
Revised: November 5, 2015

Published: November 12, 2015



isolated tungsten(VI) center bearing an oxo ligand and a carbene fragment¹⁸ (Scheme 1) is still well-accepted.^{8,19}

Scheme 1. Postulated Active Site of WO_3/SiO_2 Olefin Metathesis Catalyst



Regarding working conditions, WO_3/SiO_2 performs typically over 350 °C. This allows avoiding poisoning by (oxygenated) feed impurities, as it corresponds to both reaction and activation temperatures. An obvious strategy to increase the activity while keeping the robustness is to increase the amount of active sites and eliminate inactive oligomeric tungsten sites. Regarding the preparation of well-defined functional materials on a molecular scale, especially single-site catalysts for olefin metathesis, surface organometallic chemistry has been proven to be a powerful approach pioneered and theorized by Basset.²⁰ This methodology involves controlled grafting of a reactive organometallic precursor on a pretreated support. By judicious choice of the precursor and treatment of the support, the podality, oxidation state, and coordination environment around the metal center can be controlled. Highly active olefin metathesis catalysts, in particular those based on isolated tungsten centers, have successfully been prepared by this approach.^{8,21–30} Moreover, catalysts for other hydrocarbon transformations, such as alkane metathesis,³¹ alkyne metathesis,^{32,33} alkane dehydrogenation,³⁴ hydrogenolysis of waxes,³⁵ olefin dimerization,³⁶ trimerization³⁷ of ethylene, and polymerization,^{38,39} have also been reported.

Even though the nature of the active site of the industrially important WO_3/SiO_2 was proposed two decades ago, research on new supported group 6 transition metal (Mo, W) olefin metathesis catalysts has mainly been focused on imido systems (rather than oxo) in the past decade.^{40–42} Their straightforward preparation is simply based on a one-step protonolysis of the M–X (X = alkyl, pyrrolidyl, alkoxide) bond of known complexes (developed by Schrock et al.) on oxides. One of the earliest examples has been reported by Wolke et al.⁴³ Several years later, other groups have started to apply this approach to heterogenize organometallic olefin metathesis catalysts.^{44–46} Bearing in mind that the industrial catalyst contains an oxo ligand, we have in the last years introduced supported single-site tungsten oxo alkyl compounds as olefin metathesis precatalysts.^{21,22,47} Since available tungsten oxo alkylidene precursors are extremely limited or can only be prepared via tedious multistep procedures, we considered using simple tungsten oxo alkyl complexes. After controlled grafting and in contact with an olefinic substrate, they can undergo α -H abstraction and thus generate the required supported tungsten carbene moiety for olefin metathesis. The first well-defined supported tungsten oxo species affording olefin metathesis was prepared by grafting of the novel tungsten oxo tetraneopentyl complex that we developed onto silica dehydroxylated at 700 °C, affording monopodal tungsten oxo trineopentyl surface species.²¹ More efficiently, similar material can also be obtained by grafting of tungsten oxo trineopentyl chloride on silica dehydroxylated at 700 °C.⁴⁷ The grafting reaction of the latter precursor proceeds by protonolysis of W–Cl rather than W–C.

The striking discovery was that this class of catalysts showed an enhanced stability with time on stream in comparison to the corresponding supported imido catalyst, which deactivated rapidly in continuous flow mode by reduction of the metal through decomposition of the metallacyclobutane intermediate.²¹ Our findings were later confirmed by other research groups on the basis of a theoretical approach.⁴⁸ Inspired by these seminal works on supported tungsten oxo catalysts, other groups have newly turned their interest onto monopodally anchored tungsten on amorphous silica bearing an oxo ligand.^{19,49}

However, these are more “models of a model” rather than a true, robust, and applicable catalyst: it is obvious that the more organic ligands there are in the coordination sphere, the higher the decomposition possibilities. For instance, alkyl and alkylidene fragments readily react with C–H bonds within phenate spectator ligands as reported by Basset.⁵⁰ Thus, our approach leading to the most simple grafted species, that is, featuring only oxo spectator ligand and hydrocarbyl ligands that will be involved as catalytically active moieties, is preferable when targeting realistic models to industrial catalysts. Furthermore, the proposed active center of the industrial WO_3/SiO_2 catalyst is, rather, an isolated bipodal tungsten oxo species (Scheme 1). It is expected that this chelation will confer to the catalytic species a higher thermal stability.

Therefore, our current target is to apply surface organometallic chemistry in order to synthesize a silica material containing a bipodal tungsten oxo species as a precatalyst for olefin metathesis reactions. As will be presented below, this proved to be possible by adjusting the nature of the organometallic precursors. We demonstrate here that a simple switch of the β -substituent on the alkyl ligand (neopentyl vs neosilyl) has a dramatic effect on the outcome of the grafting, resulting in the closest analogue to date of the Phillips catalyst active site.

RESULTS AND DISCUSSION

Grafting of 1-Np onto SiO_{2-200} and Characterization of the Resulting Material. The podality of grafted species can be controlled by the dehydroxylation temperature of silica. Grafting of organometallic complexes on silica dehydroxylated at 700 °C (SiO_{2-700}) affords monopodal species.^{19,21,49,51} On the other hand, grafting on silica dehydroxylated at 200 °C (SiO_{2-200}) most frequently provides bipodal species.^{34,52,53}

A first choice of the organometallic precursor to access bipodal tungsten oxo surface species is the tungsten oxo trineopentyl chloride complex 1-Np, described by Osborn et al.⁵⁴ One of the syntheses of this complex involves hydrolysis of $[\text{W}(\equiv\text{CtBu})\text{Np}_3]$ ($\text{Np} = \text{CH}_2\text{tBu}$) to afford the trioxo alkyl dinuclear complex $[\text{O}(\text{WONp}_3)_2]$, followed by treatment with $\text{SiMe}_3\text{Cl}/\text{HCl}$.⁴⁷ As observed earlier for the tungsten oxo tetraneopentyl and tungsten oxo trineopentyl chloride systems, protonolysis could occur on W–Cl as well as on W– CH_2tBu_3 . A recent study has shown that protonolysis of W–Cl is the major pathway with a silica dehydroxylated at 700 °C. In this context, we initially envisioned that 1-Np would react with SiO_{2-200} silica first via a protonolysis reaction on W–Cl, followed by a second reaction of W– CH_2tBu_3 with an adjacent silanol that would afford a bигrafted species (Scheme S1 in the Supporting Information). The grafting of 1-Np on silica dehydroxylated at 200 °C was thus performed under dynamic vacuum, to remove HCl and shift the equilibrium toward formation of the surface species. Infrared studies show partial

consumption of the isolated silanols at 3747 cm^{-1} (Figure S1 in the Supporting Information) and growth of a large band centered at 3550 cm^{-1} , assigned to interaction of silanols with the grafted organometallic complex.

Furthermore, new peaks corresponding to typically $\nu(\text{C}-\text{H})$ and $\delta(\text{C}-\text{H})$ of alkyl fragments also appeared. Elemental analysis of the resulting material, **2-Np**, indicates W and C contents of 4.34 and C 4.08 wt %, respectively. This corresponds to a C/W molar ratio of 14.3. Furthermore, gas-phase analysis reveals that the strongly major byproduct is HCl ($215\text{ }\mu\text{mol} (\text{g of SiO}_2\text{-200})^{-1}$, quantified by IR spectroscopy), while neopentane is only marginally produced. In addition, the ^1H MAS and ^{13}C CP MAS NMR data reveal the presence of tungsten methylenic fragments, as reflected by the ^1H and ^{13}C signals at 2.0 and 91 ppm, respectively (Figure 1a and Figure S2

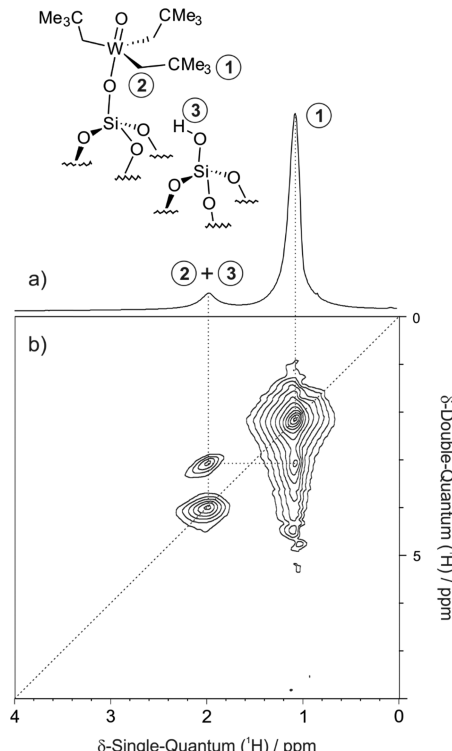
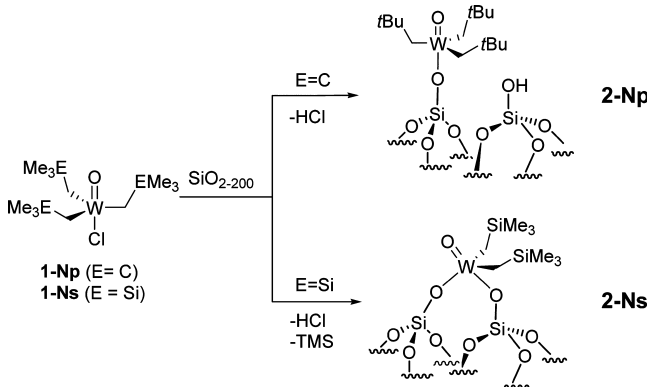


Figure 1. **2-Np:** ^1H MAS (a) and $^1\text{H}-^1\text{H}$ DQ-SQ (b) MAS NMR spectra (18.8 T, spinning speed 20 kHz).

in the Supporting Information). The $^1\text{H}-^1\text{H}$ DQ-SQ MAS NMR spectrum confirms the assignments, as the neopentyl CH_2 and CH_3 give rise to an off-diagonal correlation (Figure 1b). The silanol peak expected at about 1.8 ppm and above is masked by the methylenic proton signal (see Figure 3b for comparison).

From these combined spectroscopic and analytical elements, the reaction of **1-Np** with the $\text{SiO}_{2\text{-}200}$ leads to the monopodal surface species $[(\equiv\text{SiO})\text{WONp}_3]$ (**2-Np**) (Scheme 2). The expected W–C silanolysis step does not occur. Further heat treatment of **2-Np** up to $90\text{ }^\circ\text{C}$ in order to initiate the protonolysis of $\text{W}-\text{CH}_2\text{tBu}_3$ and access the targeted bipodal species was unsuccessful (no release of neopentane, no evolution of IR spectrum). However, when **2-Np** was treated above $90\text{ }^\circ\text{C}$, the surface complex started to decompose with formation of isobutene and methane. Such reactivity is reminiscent of tungsten aqueous organometallic chemistry

Scheme 2. Reaction of **1-Np** and **1-Ns** with $\text{SiO}_{2\text{-}200}$

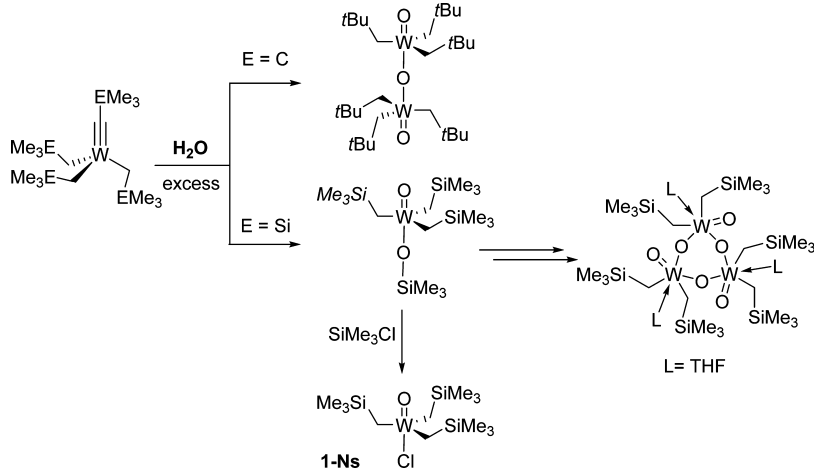


described by Schrock and Lippard.^{55,56} Indeed, the coordination environment of **2-Np** is very similar to that of the trioxo alkyl dinuclear complex $[\text{O}(\text{WONp}_3)_2]$, which is stable toward excess water (Scheme 3).

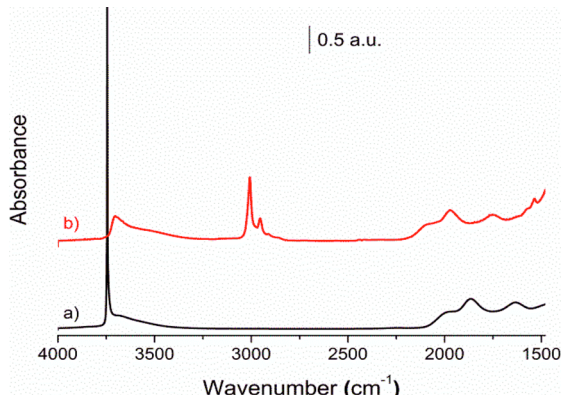
In order to push forward the second protonolysis step, the neopentyl ligand needs to be replaced by a more reactive fragment. Interestingly, Xue et al.⁵⁷ have recently studied the reactivity of $[\text{W}(\equiv\text{CSiMe}_3)(\text{CH}_2\text{SiMe}_3)_3]$ with H_2O and found a different behavior in comparison to $[\text{W}(\equiv\text{CtBu})\text{Np}_3]$. When $[\text{W}(\equiv\text{CSiMe}_3)(\text{CH}_2\text{SiMe}_3)_3]$ reacts with water, the authors observed mainly two products: a tungsten dioxo bis-neosilyl trimer and $[\text{WO}(\text{OSiMe}_3)(\text{CH}_2\text{SiMe}_3)_3]$ (Scheme 3).

The yield of both products is dependent on the synthesis temperature and the quantity of water. This finding has shown that a tungsten alkyl–alkylidyne bearing neosilyl ligands can readily undergo multiple hydrolysis by water, in contrast to the tungsten neopentyl complex that hydrolyzes only once (that is, in which only a single W–C fragment is affected), forming a stable dinuclear complex. Thus, we reasoned that the tungsten oxo trineosilyl chloride $[\text{WOCl}(\text{CH}_2\text{SiMe}_3)_3]$ (**1-Ns**) is clearly an attractive organometallic precursor that may provide bipodal tungsten oxo bis-alkyl surface species after grafting onto a silica dehydroxylated at $200\text{ }^\circ\text{C}$. We then established the synthesis of this new complex $[\text{WOCl}(\text{CH}_2\text{SiMe}_3)_3]$ (**1-Ns**). It was obtained in 70% yield from $[\text{W}(\equiv\text{CSiMe}_3)(\text{CH}_2\text{SiMe}_3)_3]$ by hydrolysis at $-78\text{ }^\circ\text{C}$ with 2 equiv of H_2O in THF (resulting in formation of the unstable intermediate $[\text{WO}(\text{OSiMe}_3)(\text{CH}_2\text{SiMe}_3)_3]$ as reported by Xue) followed by reaction with 2 equiv of Me_3SiCl (Scheme 3). Alternatively, we also found that **1-Ns** can be more straightforwardly accessed in two steps from WOCl_4 : tungsten oxotetrachloride reacts with neopentanol to afford $[\text{WOCl}_3(\text{ONp})]$, which is reacted in situ without a purification step with commercial neosilyl Grignard reagent (3 equiv). The nonoptimized yield is 15%. NMR features indicate the presence of equivalent neosilyl moieties, with the methylenic group giving rise to a singlet at 2.3 ppm ($J_{\text{W}-\text{H}} = 11.0\text{ Hz}$), 76 ppm ($J_{\text{W}-\text{C}} = 85.1\text{ Hz}$), and 0.9 ppm in the ^1H , ^{13}C , and ^{29}Si NMR spectra, respectively. These elements are in line with a structure similar to that of the neopentyl analogue **1-Np**, namely a trigonal bipyramidal, with the oxo and chloride occupying the axial positions.

Grafting of **1-Ns onto $\text{SiO}_{2\text{-}200}$ and Characterization of the Resulting Material.** The grafting of colorless **1-Ns** on silica dehydroxylated at $200\text{ }^\circ\text{C}$ was performed under dynamic vacuum at $80\text{ }^\circ\text{C}$. **1-Ns** reacts readily with silica dehydroxylated at $200\text{ }^\circ\text{C}$, to afford a pale yellow material (interestingly, **2-Np** is colorless). Infrared studies show quasi-quantitative con-

Scheme 3. Hydrolysis of $[W(\equiv CEMe_3)(CH_2EMe_3)]$ ($E = C, Si$) and Synthesis of 1-Ns

sumption of the noninteracting silanols (3747 cm^{-1}), while new, broad bands appear at 3690 and at about 3530 cm^{-1} , characteristic of perturbed SiOH (Figure 2).

**Figure 2.** FT-IR spectra of SiO_{2-200} (a) and 2-Ns (b).

Furthermore, new peaks corresponding to $\nu(\text{C}-\text{H})$ of alkyl fragments also appeared. Elemental analysis indicates W and C contents of 5.72 and 3.15 wt %, respectively. This corresponds to a C/W molar ratio of 8.4. Furthermore, gas-phase analysis upon grafting indicates release of HCl ($310\text{ }\mu\text{mol} (\text{g of } \text{SiO}_{2-200})^{-1}$, quantified by IR spectroscopy). Tetramethylsilane was qualitatively detected, but gas-phase analyses proved to be unrepeatable. When the released TMS was trapped in an NMR tube containing C_6D_6 and ferrocene as an internal standard, 0.85 TMS/W was observed (Figure S3 in the Supporting Information). Thus, the characterization elements are in line with the formation of the major bipodal species $[(\equiv \text{SiO})_2\text{WO}(\text{CH}_2\text{SiMe}_3)_2]$ (2-Ns) (Scheme 2).

Furthermore, the ^1H MAS, ^{13}C CP MAS, and ^{29}Si CP MAS NMR data are in full agreement with such a conclusion. More specifically, the methylenic fragments give rise to ^1H and ^{13}C signals at 1.55 and 65 ppm in the ^1H and ^{13}C spectra, respectively (Figures 3a and 4a). For comparison, the oxo bis-alkyl complex $[\{\text{W}(\text{O})(\mu-\text{O})(\text{Ns})_2(\text{THF})\}_3]$ gives rise to signals at 1.85 and 70 ppm in ^1H and ^{13}C NMR, respectively.⁵⁷ The ^{29}Si MAS NMR spectrum exhibits two signals at 2.1 and -100 ppm, accounting for the neosilyl ligand and the silica support,⁵⁸ respectively (Figure 4b).

The $^1\text{H}-^1\text{H}$ DQ-SQ MAS NMR spectrum features several off-diagonal correlations (Figure 3b). The correlation A associates the CH_2 and CH_3 protons from the neosilyl ligands, respectively, at 1.5 and 0.1 ppm in the single-quantum (SQ) dimension. Correlation B is assigned to interaction between silanols and methyl protons (respectively at 1.8–2.7 and 0.1 ppm). Accordingly, correlation C involves silanols and CH_2 protons. The shifted silanol pattern is in line with observations from infrared measurements, as unperturbed SiOH resonates at 1.8 ppm.

DFT Calculations. To gain further insights into the experimental data described above, DFT calculations were carried out to confirm and refine the understanding of the grafting reaction of complex 1-Ns onto silica dehydroxylated at $200\text{ }^\circ\text{C}$ (SiO_{2-200}). In a continuation of previous theoretical studies,^{59–64} we considered as surface models two cagelike polyoligosilosylesquioxane derivatives (Figure 5), called **b** and **ac** models. The two upper silicon atoms reproduce the emerged part of the silica surface: i.e., a combination of vicinal silanol groups connected by a hydrogen bond (**b** model) or by a siloxane bridge (**ac** model), as observed on a silica surface dehydroxylated at $200\text{ }^\circ\text{C}$. This is surrounded by a layer built around four silicon atoms, themselves surrounded by another layer formed by two silicon atoms added in order to increase the rigidity of the model. Both silicon atoms are connected to hydroxyl groups in order to saturate the model. In the same way, SiH_3 groups are added on the emerged part of the silica, to saturate the lateral siloxane bridges formed during the dehydroxylation reaction of the silica surface.

To shed light on the grafting reaction of complex 1-Ns onto SiO_{2-200} , the W–Cl silanolysis with the concomitant HCl production and the W–C_{Ns} silanolysis leading to the production of free TMS have been considered. The Gibbs free energy profiles of both grafting reactions on the two considered silica surface models are depicted in Figure 6. The key geometrical parameters of the different stationary points are gathered in Tables S1 and S2 in the Supporting Information.

The grafting reaction begins by the formation of endergonic adducts A^b_{HCl} and $\text{A}^{\text{ac}}_{\text{HCl}}$ (W–Cl silanolysis on **b** and **ac** models, respectively; Figure S4 in the Supporting Information) and A^b_{TMS} and $\text{A}^{\text{ac}}_{\text{TMS}}$ (W–Ns silanolysis on **b** and **ac** models, respectively; Figure S5 in the Supporting Information), located respectively between 21.6 and 22.9 kcal mol⁻¹ and between 11.4 and 13.7 kcal mol⁻¹ with respect to the separated

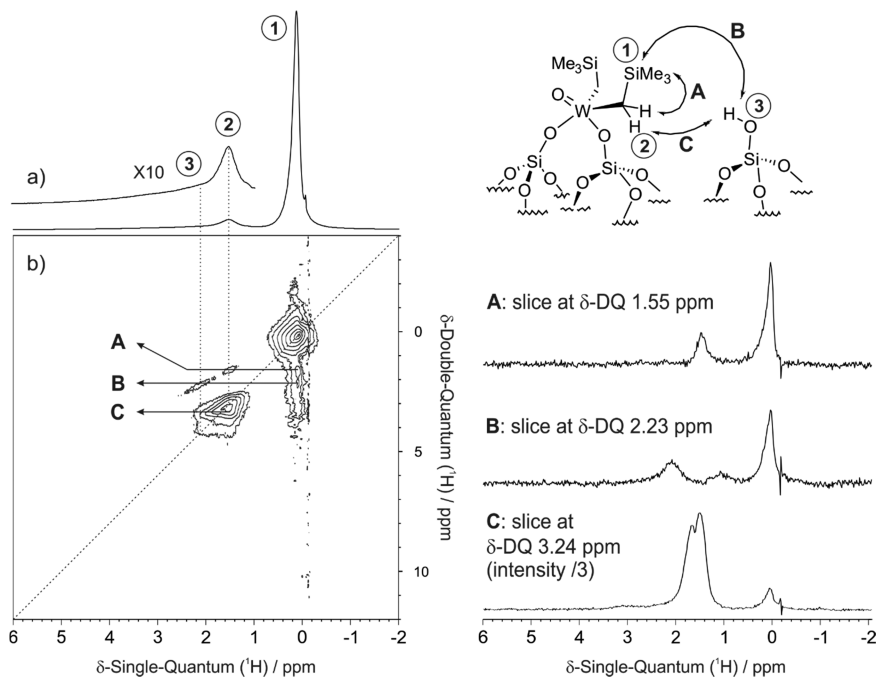


Figure 3. 2-Ns: (a) ^1H MAS and (b) ^1H - ^1H DQ-SQ MAS NMR spectra (18.8 T, spinning speed 20 kHz), along with assignments and selected correlations.

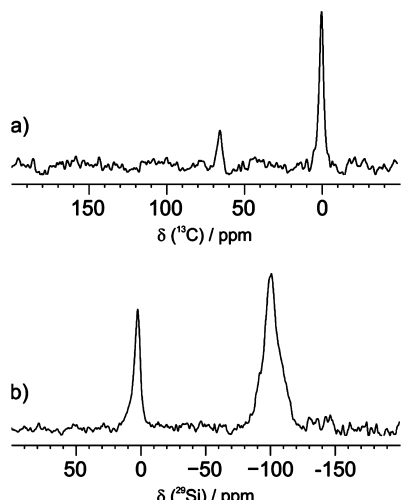


Figure 4. 2-Ns: ^{13}C (a) and ^{29}Si (b) CP MAS NMR spectra (11.75 T).

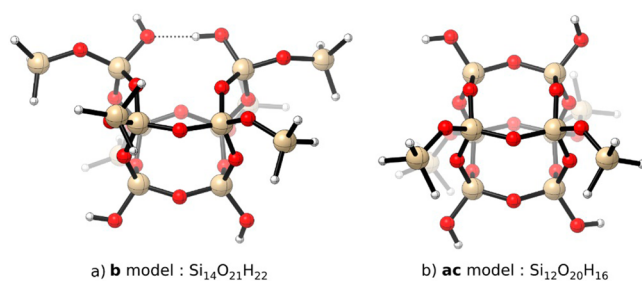


Figure 5. Representation of the two systems used as models of a silica surface dehydroxylated at 200 °C.

reactants. These different adducts are obtained by an IRC calculation. This stability difference is mainly due to the interaction between the organometallic compound and the surface models. Indeed, for $\text{A}^{\text{b}}_{\text{TMS}}$ and $\text{A}^{\text{ac}}_{\text{TMS}}$, the structure of

the $[\text{WONs}_3\text{Cl}]$ moiety is almost identical with that of the free complex. The endergonic formation of these adducts, and even more for $\text{A}^{\text{b}}_{\text{HCl}}$ and $\text{A}^{\text{ac}}_{\text{HCl}}$, corresponds also to the loss of translational entropy due to the molecular association as well as the formation of a slightly less stable isomer of 1-Ns. Indeed, the interaction between the oxygen atom of the silanol and the metal center induces an energetically costly Berry pseudorotation of $[\text{WONs}_3\text{Cl}]$ from a trigonal-bipyramidal to a square-pyramidal geometry. One W-Cl is slightly elongated (by 0.1 Å), with the chloride atom pointing toward the hydrogen atom of the silanol. From $\text{A}^{\text{b}}_{\text{HCl}}$ and $\text{A}^{\text{ac}}_{\text{HCl}}$, the W-Cl silanolysis reaction leading to the formation of monografted tungsten oxo trineosilyl $2^{\text{b}}\text{-Ns}_{\text{mono}}$ and $2^{\text{ac}}\text{-Ns}_{\text{mono}}$ complexes (Figure 7), with concomitant formation of one free HCl molecule, is a slightly endergonic process (between 3.5 and 8.8 kcal mol⁻¹ with respect to the separated reactants). From a kinetic point of view, the activation barrier for the W-Cl silanolysis reaction is relatively low (between 26.2 and 28.3 kcal mol⁻¹ with respect to the separated reactants). Scrutinizing the geometrical features of these transition states, one can observe that their structures remain similar to those of adducts which they are connected, in good agreement with their small Gibbs free energy difference. For the two transition states, the $W-\text{OSi}\equiv$ distance is shortened in comparison to the adducts (by around 0.2 Å) whereas the $W-\text{Cl}$ and $H-\text{OSi}\equiv$ distances are elongated (by around 0.5 and 0.07 Å, respectively). The products of this step are two transient species, located between +15.1 and +18.4 kcal mol⁻¹ with respect to the entrance channel, according to the considered surface model. At these intermediates, as revealed by the second-order perturbation NBO analysis, the HCl molecule remains in interaction with the oxygen atom, which ensures the grafting of the tungsten complex onto the silica surface. The removal of HCl leads to the formation of the aforementioned monografted products $2^{\text{b}}\text{-Ns}_{\text{mono}}$ and $2^{\text{ac}}\text{-Ns}_{\text{mono}}$. From a geometrical point of view, in both cases the tungsten atom adopts a slightly distorted trigonal

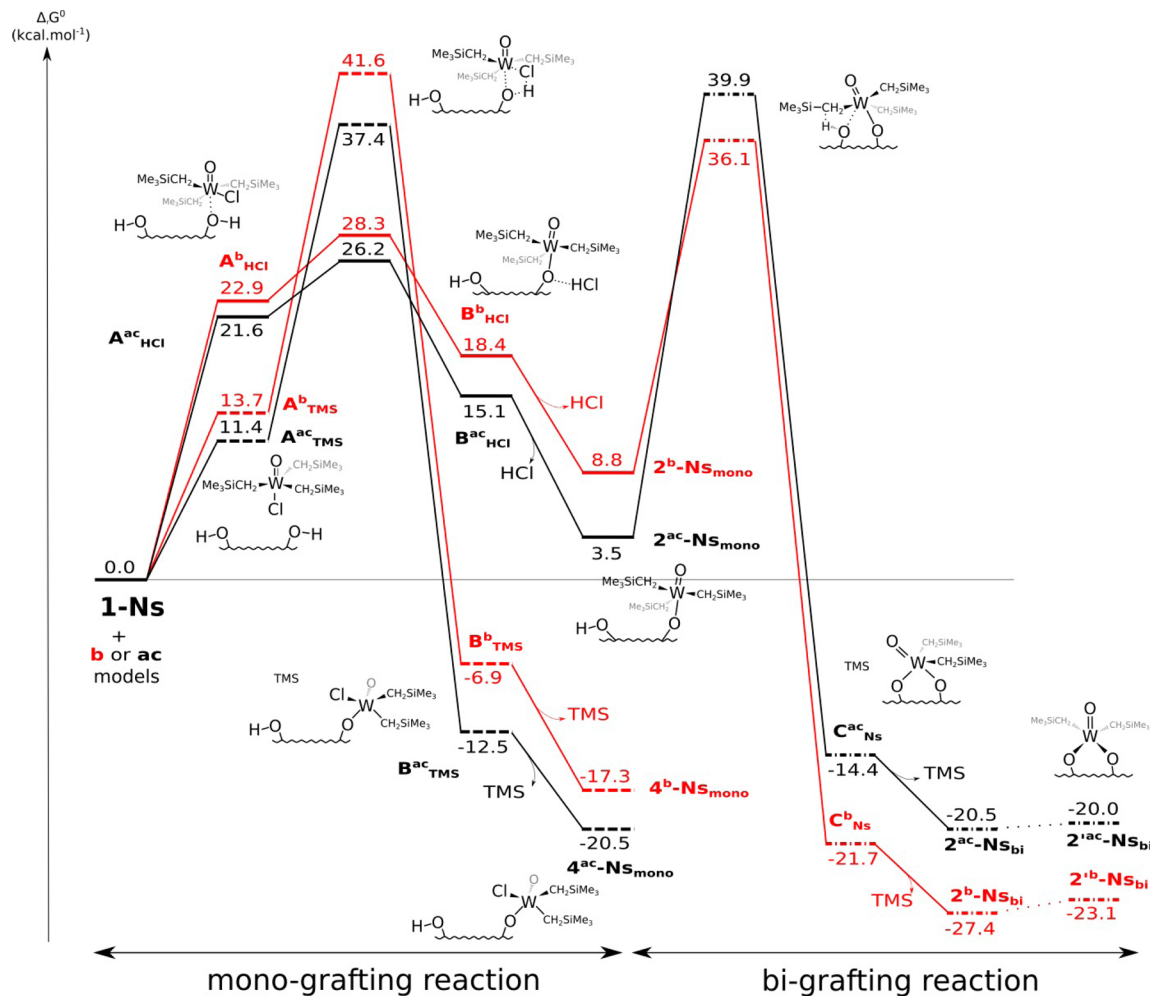


Figure 6. Gibbs free energy profile (in kcal mol^{-1}) for the grafting reaction of **1-Ns** onto **a** and **b** SiO_2 -200 surface models.

bipyramidal geometry with the three neosilyl ligands in equatorial sites ($W-\text{CH}_2\text{SiMe}$ distances around 2.10 Å) with the oxo and the oxygen atom of the silica surface occupying the two axial sites ($W=\text{O}$ and $W-\text{OSi}\equiv$ distances around 1.71 and 2.10 Å, respectively).

On the other hand, from **A^b TMS** and **A^{ac} TMS**, the $W-\text{C}_{\text{Ns}}$ silanolysis reaction proceeds with an activation barrier between 37.4 and 41.6 kcal mol⁻¹ with respect to the separated reactants, according to the considered surface model. The formation of the final tungsten oxo dineosilyl chloride complexes **4^b-Ns_{mono}** and **4^{ac}-Ns_{mono}** (Figure 7), with concomitant formation of one free TMS molecule, is an exergonic process (between -17.3 and -20.5 kcal mol⁻¹ with respect to the separated reactants). In **4^b-Ns_{mono}** and **4^{ac}-Ns_{mono}**, the tungsten atom adopts a distorted-square-pyramidal geometry with an oxo ligand occupying the apical position. It is noteworthy that the transition states of the $W-\text{C}_{\text{Ns}}$ silanolysis are roughly 12 kcal mol⁻¹ higher in energy than those of the $W-\text{Cl}$ silanolysis. This difference can be explained by the electrostatic effects, since the greater steric hindrance around the metal center in $\text{TS}(\text{A}^{\text{b/ac}} \rightarrow \text{B}^{\text{b/ac}})$ than in $\text{TS}(\text{A}^{\text{b/ac}} \rightarrow \text{B}^{\text{b/ac}})$ destabilizes the system due to the electrostatic repulsion between the silica surface and the neosilyl ligands. Thus, in agreement with the experiments, as for the monografting of a oxo trineopentyl chloride complex onto an isolated silanol group (**c** model⁴⁷), the monografting

reaction of **1-Ns** onto **b** and **ac** models proceeds via the cleavage of the $W-\text{Cl}$ bond and not by $W-\text{C}$ silanolysis, affording $[\equiv\text{SiOWONs}_3]$ surface species.

Finally, the mechanistic investigation of the grafting reaction of **1-Np** onto **b** and **ac** models was also performed, in order to rationalize the experimental observations done with this compound as described above. As can be seen in Table S3 in the Supporting Information and in Figure 8, the relative Gibbs free energies of the intermediates and the activation barriers involved in the monografting reaction of **1-Np** onto **b** and **ac** models are similar to those obtained for the monografting process of **1-Ns** onto the same models. As for **1-Ns**, the monografting reaction proceeds via the cleavage of the $W-\text{Cl}$ bond, and not by $W-\text{C}$ silanolysis, affording $[\equiv\text{SiOWONp}_3]$ surface species. The formation of **2^b-Np_{mono}** and **2^{ac}-Np_{mono}** is an almost athermic process (+2.8 and +1.2 kcal mol⁻¹ with respect to the entrance channel), which takes place through accessible activation barriers calculated to be +24.3 and +21.3 kcal mol⁻¹ with respect to the separated reactants (Table S3 and Figure 8).

The key element emerging from experimental evidence is the bigrafting reaction observed in the case of neosilyl ligands only. Thus, in the DFT-calculated mechanism, from **2^b-Ns_{mono}**, **2^{ac}-Ns_{mono}**, **2^b-Np_{mono}**, and **2^{ac}-Np_{mono}** the subsequent step corresponds to the bigrafting reaction through $\text{TS}(2^{\text{b}}\text{-Ns}_{\text{mono}} \rightarrow \text{C}^{\text{b}}_{\text{Ns}})$, $\text{TS}(2^{\text{ac}}\text{-Ns}_{\text{mono}} \rightarrow \text{C}^{\text{ac}}_{\text{Ns}})$, $\text{TS}(2^{\text{b}}\text{-Np}_{\text{mono}} \rightarrow$

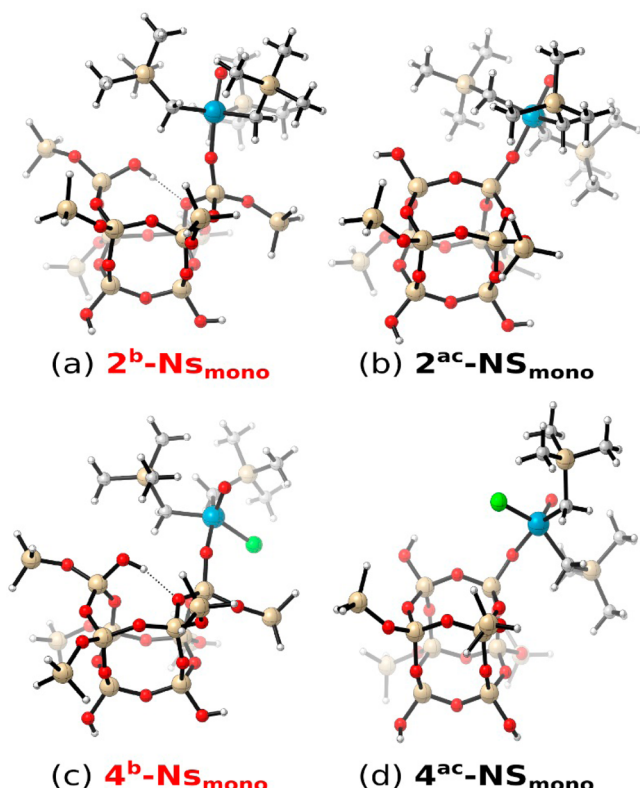


Figure 7. Optimized structures of monografted complexes involved in the grafting reaction of **1-Ns** onto **b** and **ac** models.

C_{Np}^b), and $TS(2^{ac}-Np_{mono} \rightarrow C_{Np}^{ac})$, respectively. For the neopentyl systems, the activation Gibbs-free energies for this reaction are $42.0\text{ kcal mol}^{-1}$ ($TS(2^b-Np_{mono} \rightarrow C_{Np}^b)$) and $45.2\text{ kcal mol}^{-1}$ ($TS(2^{ac}-Np_{mono} \rightarrow C_{Np}^{ac})$) with respect to the entrance channel. In both cases, in agreement with experimental results, the high energy barriers make the bigrafting reactions unlikely to occur. From 2^b-Ns_{mono} and 2^{ac}-Ns_{mono} , the activation barrier of the bigrafting reaction lies at $36.1\text{ kcal mol}^{-1}$ ($TS(2^b\text{-Ns}_{mono} \rightarrow C_{Ns}^b)$) and $39.9\text{ kcal mol}^{-1}$ ($TS(2^{ac}\text{-Ns}_{mono} \rightarrow C_{Ns}^{ac})$) above the separated reactants, which corresponds to a highly demanding but accessible process. This is summarized in **Table 1**.

The computed activation energy difference is around 6 kcal mol^{-1} in favor of neosilyl ligands (**Table 1**), which is above the uncertainty of the DFT calculations (of about 3 kcal mol^{-1}).^{65,66} This difference between neopentyl and neosilyl compounds can be explained by a difference in the charge alternation at the transition states (**Figure 9**). Remarkably, the DFT-calculated difference in energetic barriers for a given SiO_{2-200} model (**ac** or **b**) is well in line for the experimentally observed reactivity difference. In agreement with the common chemical belief that a silicon center strongly stabilizes an α -negative charge and a β -positive charge, the negative charge of the CH_2 carbon is strongly stabilized by the presence of the silicon atom, leading to a better charge alternation at the transition state and consequently a decrease of the activation barriers.

The products of this step are the two bigrafted transient intermediates C_{Ns}^{ac} and C_{Ns}^b , located between -14.4 and $-21.7\text{ kcal mol}^{-1}$ with respect to the entrance channel. The removal of the free TMS leads to the final 2^{ac}-Ns_{bi} and 2^b-Ns_{bi} products (**Figure 10**). This step is exergonic, with Gibbs free

energies of $-20.5\text{ kcal mol}^{-1}$ (2^{ac}-Ns_{bi}) and $-26.8\text{ kcal mol}^{-1}$ (2^b-Ns_{bi}), with respect to the entrance channel. The stability difference between both products may be explained by the rigidity of the vicinal anchoring sites on the **ac** model due to the presence of a siloxane bridge between the vicinal silanol groups. In both cases, the bigrafted tungsten complex exhibits a slightly distorted trigonal bipyramidal geometry with the two neosilyl ligands and the oxygen atom of the silica surface involved in the bigrafting process in equatorial sites ($W-\text{CH}_2\text{SiMe}$ and $W-\text{OSi}\equiv$ distances around 2.10 and 1.99 \AA , respectively) and the oxo and the second oxygen atom of the silica surface occupying the two axial sites ($W=\text{O}$ and $W-\text{OSi}\equiv$ distances around 1.71 and 1.88 \AA , respectively).

It is noteworthy that an equilibrium is observed between the two trigonal-bipyramidal 2^{ac}-Ns_{bi} and 2^b-Ns_{bi} and two distorted-square-pyramidal $2'^{ac}\text{-Ns}_{bi}$ and $2'^b\text{-Ns}_{bi}$ conformations. In $2'^{ac}\text{-Ns}_{bi}$ and $2'^b\text{-Ns}_{bi}$, the two anchoring oxygen atoms and two neosilyl ligands occupy the basal positions in a *cis* configuration ($W-\text{CH}_2\text{SiMe}$ around 2.14 \AA and $W-\text{OSi}\equiv$ distances around 1.93 \AA) with an oxygen atom in the axial position ($W=\text{O}$ distances of 1.692 and 1.691 \AA , respectively, for $2'^b\text{-Ns}_{bi}$ and $2'^{ac}\text{-Ns}_{bi}$). These distorted-square-pyramidal forms are marginally higher in energy ($+0.5$ and $+3.3\text{ kcal mol}^{-1}$, respectively, with respect to 2^{ac}-Ns_{bi} and 2^b-Ns_{bi}) and are connected to the trigonal-bipyramidal forms via a low activation barrier (roughly 5 kcal mol^{-1}). This dynamic behavior will have an effect on NMR features, most particularly regarding ^{17}O NMR studies, as described below.

Experimental and Theoretical Approaches to ^{17}O NMR

In the course of different studies, we have demonstrated that ^{17}O NMR is an efficient tool for the study of molecular and supported oxo species.^{22,47} Indeed, for systems analogous to those considered here, upon selective ^{17}O labeling of the oxo moiety, we have seen that their ^{17}O MAS NMR spectra feature highly characteristic line shapes. When these results were coupled to DFT calculations, it was also possible to assess the local structure of the grafted organometallic center. In the present case, we used this methodology to study materials **2-Np-O*** and **2-Ns-O*** (corresponding to **2-Np** and **2-Ns** featuring a ^{17}O -enriched $W=\text{O}$ moiety). As reported in previous studies, their ^{17}O MAS NMR spectra result from the combination of large quadrupolar and chemical shift anisotropy (**Figure 11**). The corresponding sets of NMR parameters were obtained from best fit simulations. They are in good agreement with DFT-calculated values (**Table S4** in the Supporting Information).

The chemical shift (CS) is the most affected parameter when NMR features of mono- and bigrafted species are compared. The CS of **2-Ns** is 15 ppm higher than that of **2-Np** (respectively 766 and 751 ppm). Despite the significant change within the W coordination sphere, the chemical shift anisotropy and quadrupolar coupling are highly similar between the two structural types.

When comparing the neopentyl derivative **2-Np** and that of the material derived from grafting of the same precursor on SiO_{2-700} (designated as **1-Np/SiO₂₋₇₀₀** in **Tables S4** and **S5** in the Supporting Information), one clearly sees that only CS is decreased by about 6 ppm (751 vs 757 ppm , respectively), while C_Q is unchanged, to 5.3 MHz (in line with a similar geometry). This shielding is confirmed by DFT calculations, where structures featuring neighboring silanols typically afford lower CS values in comparison to structures on purely isolated silica models (2^b-Np_{mono} and 2^{ac}-Np_{mono} ; **Table S4**).

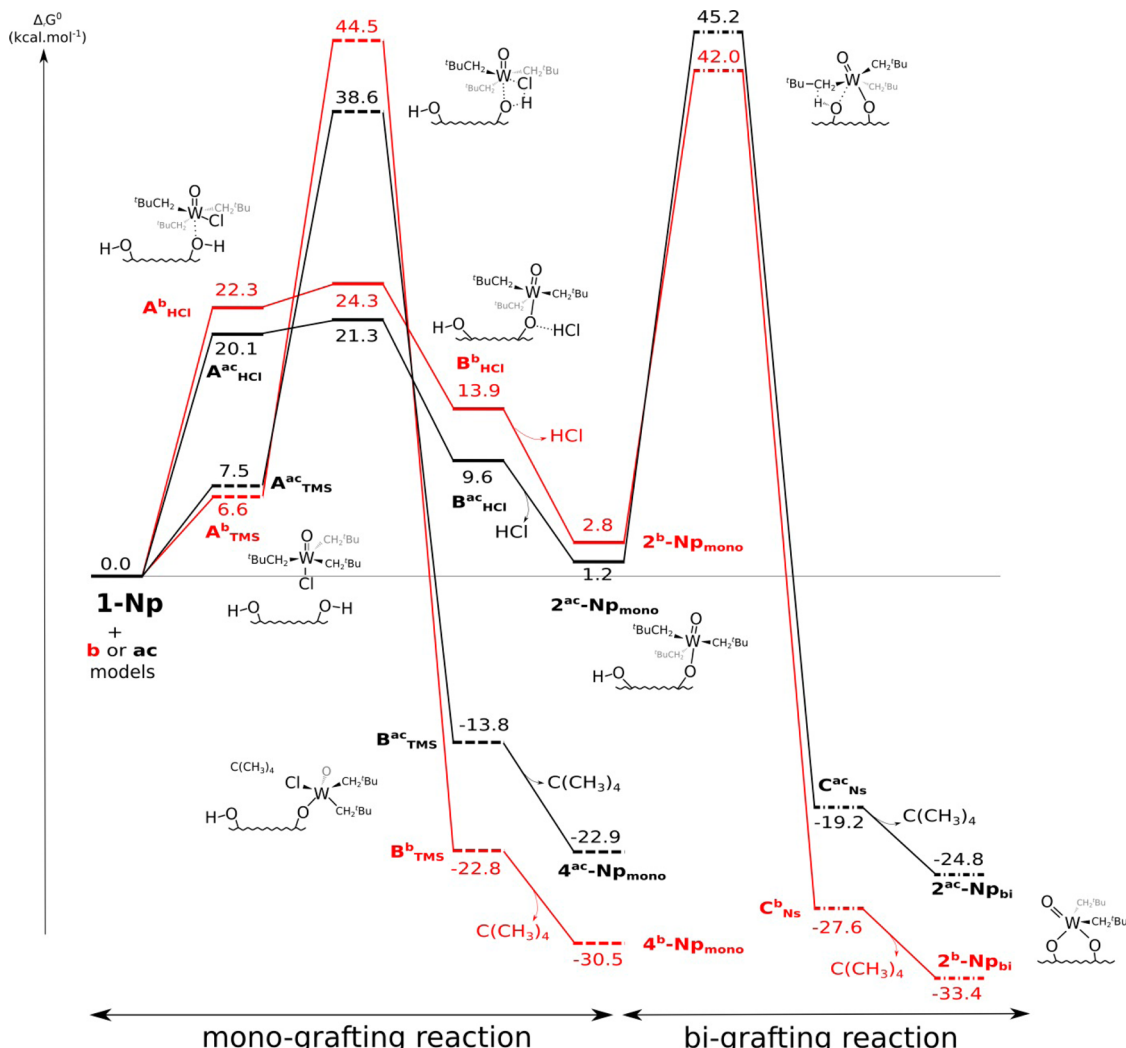


Figure 8. Gibbs free energy profile (in kcal mol^{-1}) for the grafting reaction of **1-Np** onto **a** and **b** $\text{SiO}_2\text{-}200$ surface models.

Table 1. Energy Barrier of the W–C Silanolysis Corresponding to the Mono- to Bi-Grafted Species Evolution (kcal mol^{-1} with Respect to Entrance Channel)

	Ns	Np	diff in energy (Ns vs Np)
ac model	39.9	45.2	-5.3
b model	36.1	42.0	-5.9

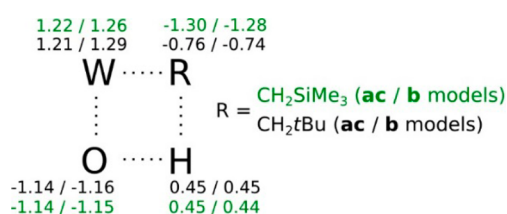


Figure 9. Natural charges of the atoms involved in the bigrafting reaction in $\text{TS}(2^{b/\text{ac}}\text{-Ns}_{\text{mono}} \rightarrow \text{C}^{b/\text{ac}}_{\text{Ns}})$ (in green) and $\text{TS}(2^{b/\text{ac}}\text{-Np}_{\text{mono}} \rightarrow \text{C}^{b/\text{ac}}_{\text{Np}})$ (in black).

Regarding **2-Ns**, NMR parameters (CS and C_Q values of 766 ppm and 5.5 MHz) fit mostly with a DFT trigonal-bipyramidal type structure, with the oxo ligand and a siloxide being in the apical positions (namely, average CS and C_Q values of 784 ppm and 5.4 MHz, respectively, for two different $\text{SiO}_2\text{-}200$ models;

Figure 10 and Table S4 in the Supporting Information). However, as seen from DFT calculations, the energetically accessible square-pyramidal form (average CS and C_Q values of 709 ppm and 1.8 MHz, respectively, for two different $\text{SiO}_2\text{-}200$ models; Figure 10 and Table S4) may be responsible for the observed CS value being lower than the calculated value.

As a further option to probe the use of ^{17}O NMR as a tool for grafted species studies, we resorted to the selective ^{17}O surface labeling of the surface itself, as reported previously.⁶⁷ We prepared **2-Np-SiO₂*** and **2-Ns-SiO₂*** (corresponding respectively to grafting of **1-Np** and **1-Ns** on $\text{SiO}_2\text{-}200$ that was selectively surface-enriched in ^{17}O as previously described) following the same procedure as described above for non-labeled silica. The ^{17}O MAS NMR spectra are displayed in Figure 12.

The main difference between the spectra of both materials is the lower intensity of the silanol peak (10 ppm) in the case of **2-Ns-SiO₂***, as expected from the formation of the bipodal species that consumes a further 1 equiv of silanol. The silanol peaks are significantly shifted in comparison to the silanols on $\text{SiO}_2\text{-}700$ (10 ppm vs -4 ppm, respectively), which indicates a significant perturbation of the electronic environment of SiOH groups.

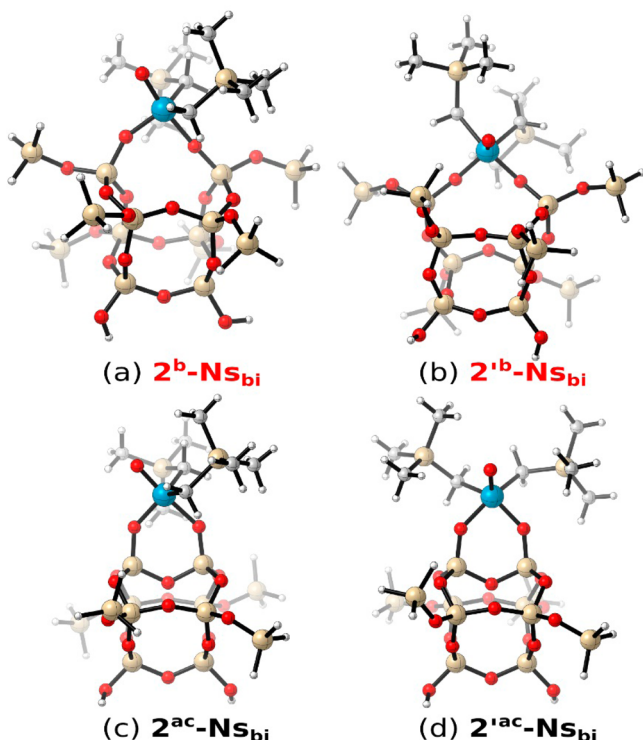


Figure 10. Optimized structures of bигrafted complexes involved in the grafting reaction of **1-Ns** onto **b** and **ac** models.

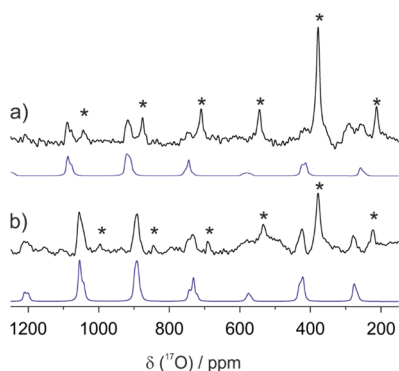


Figure 11. ^{17}O MAS NMR spectra and corresponding best fit simulations of (a) 2-Ns-O^* (18.8 T, spinning speed 18 kHz) and (b) 2-Np-O^* (21.15 T, spinning speed 19 kHz).

The chemical shift of $\text{W}-\text{O}-\text{Si}$ for both species are close (157 ppm for 2-Np-SiO_2^* , to be compared to 168 ppm for 2-Ns-SiO_2^*). The width of the signal is similar for both samples. Best fit simulations were performed, using the Czjzeck model, with an average C_Q value of about 2.6 MHz and a chemical shift distribution of 18 ppm. This was confirmed by comparison with the spectra recorded at lower magnetic field (9.4 T). The good fit using the Czjzeck model is an indication that the SiOW resonance line shapes are dominated by a combination of C_Q and chemical shift distributions.^{68,69} On comparison to DFT-calculated values (Table S5 in the Supporting Information), if the CS is within the expected range, the theoretical C_Q values are significantly higher than the experimental ones (3.8–5.3 vs 2.6 MHz, respectively). The origin of this discrepancy is poorly understood at this stage. In a more general point of view, the 1D ^{17}O NMR data for these systems (with either $\text{W}=\text{O}$ or silica surface labeling) do not allow us to unambiguously

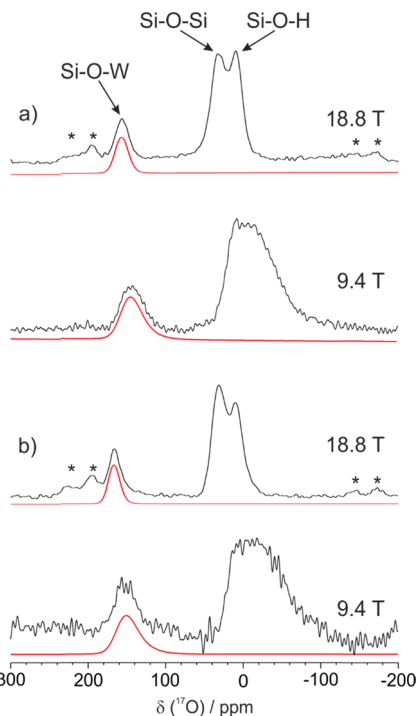


Figure 12. ^{17}O MAS NMR of (a) 2-Np-SiO_2^* and (b) 2-Ns-SiO_2^* at 9.4 and 18.8 T (spinning speed 20 kHz). The red lines are the simulated lines for the siloxide oxygen. Asterisks indicate spinning sidebands.

determine the hapticity of the surface toward the organometallic center, in contrast to what was observed for other tungsten oxo systems.²²

In order to get further insight into the various types of surface oxygen environments in 2-Ns-SiO_2^* , the MQ MAS spectrum was recorded (Figure 13). We can distinguish among the three different types of oxygen-containing surface groups: (1) the silanols that feature a low C_Q value and that are present as a chemical shift distributed signal (from 5 to 13 ppm), (2) the siloxanes that give rise to a pattern indicative of strongly quadrupolar-coupled sites (at 37 ppm, with a C_Q of about 5.4 MHz), along with very narrow CS distribution, and (3) the $\text{W}-\text{O}-\text{Si}$ sites that are present as CS-distributed signals (175–160 ppm) with an estimated C_Q value of 2.8 MHz, as deduced from the position of the signal with respect to the 1:1 diagonal (dotted line in Figure 13). The values observed here for the WOSi moieties are in line with those extracted from the 1D spectra at 9.4 and 18.8 T (Figure 12).

In comparison to our previous results obtained in the case of the MQ MAS spectrum of ^{17}O -surface-labeled SiO_{2-200} and of $[\text{W}(\equiv \text{CtBu})\text{Np}_3]$ grafted on ^{17}O -surface-labeled SiO_{2-200} ,⁶⁷ the siloxane signal is close to that of pristine SiO_{2-200} . This is well in line with the EXAFS results, which do not provide indication of an SiOSi interaction with the tungsten center (vide infra). On the other hand, the signal of residual silanols is perturbed to the same extent as for $[\text{W}(\equiv \text{CtBu})\text{Np}_3]$ grafted on SiO_{2-200} .

The $^1\text{H}-^{17}\text{O}$ D-HMQC spectrum of both 2-Ns-SiO_2^* and 2-Np-SiO_2^* samples has been recorded (Figure 14 and Figure S6 in the Supporting Information). The most intense correlation for both samples is that of the $\text{SiO}-\text{H}$ fragment, which extends up to about 3.5 ppm in the ^1H dimension. In the case of 2-Np-SiO_2^* , this confirms that the ^1H NMR signal from the SiOH protons is indeed masked by that of the WCH_2 .

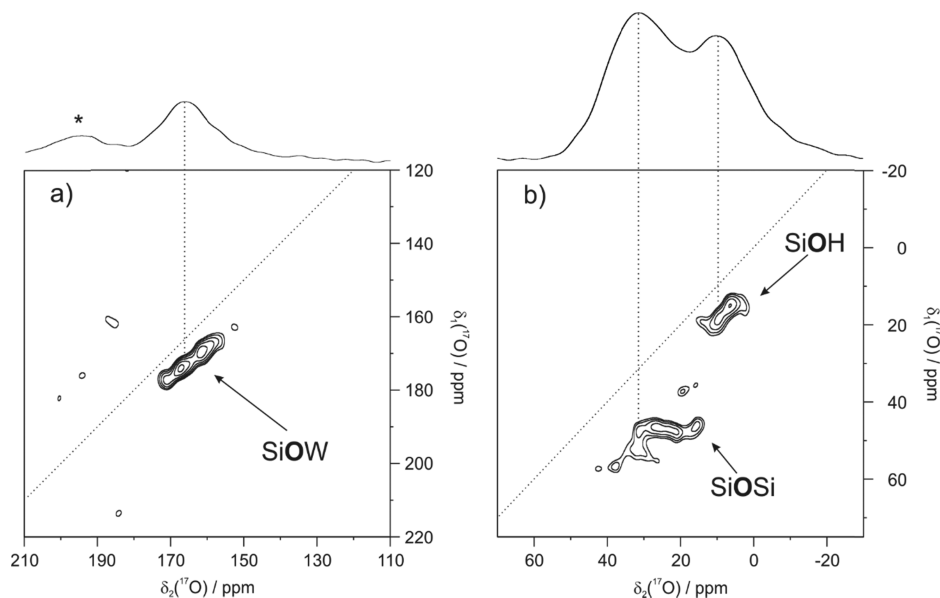


Figure 13. ^{17}O MQ MAS NMR of 2-Ns-SiO* in (a) the SiOW region and (b) in the SiOH and SiOSi region (18.8 T, 20 kHz).

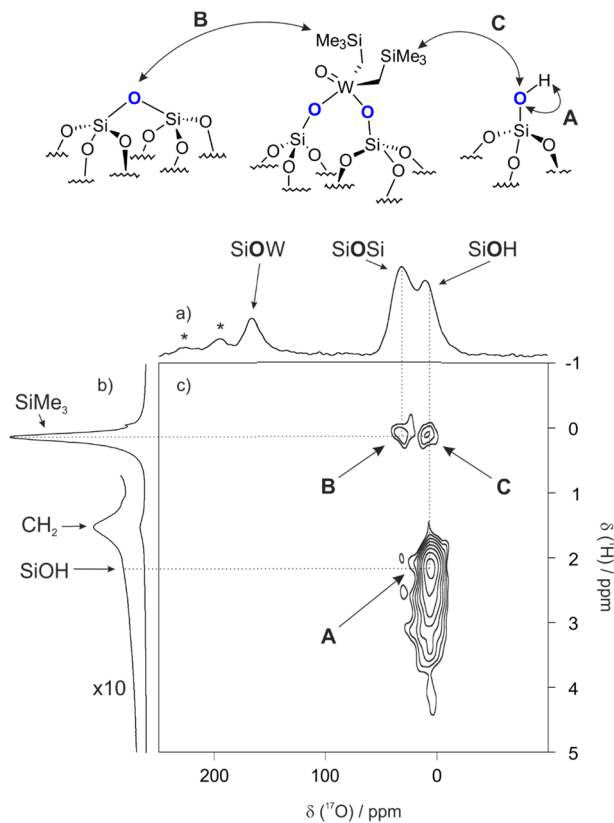


Figure 14. 2-Ns-SiO*: (a) ^{17}O MAS, (b) ^1H MAS, and (c) $^1\text{H}-^{17}\text{O}$ D-HMQC MAS NMR spectra (18.8 T, spinning speed 20 kHz; asterisks indicate spinning sidebands).

Regarding 2-Ns-SiO₂*^{*}, two significantly weaker correlations involve the silanols and siloxane oxygens (^{17}O 10 and 31 ppm, respectively) with the protons from the neosilyl ligand methyl groups (^1H 0.0 ppm). The fact that such interaction is observed in the case of bipodal 2-Ns-SiO₂*^{*} and not of monopodal 2-Np-SiO₂*^{*} can be ascribed to restricted mobility enforced by the bipodal configuration. The higher mobility of monopodal species in 2-Np-SiO₂*^{*} would then be detrimental to the

$^1\text{H}-^{17}\text{O}$ heteronuclear dipolar exchange that provides a signal in the $^1\text{H}-^{17}\text{O}$ D-HMQC spectrum.

EXAFS Studies on 2-Ns. The structural hypothesis for the grafted species 2-Ns was further confirmed by an XAS study. This consisted of recording and analyzing the W L_{III}-EXAFS spectra of both the molecular complex 1-Ns and the supported species resulting from its grafting onto SiO₂₋₂₀₀ in order to assess and compare the structures of the tungsten coordination sphere in both cases.

For 1-Ns (Figure 15 and Table 2), the results are consistent with the following coordination sphere around W: one oxygen atom at 1.694(8) Å, assigned to an oxo ligand, ca. three carbons at 2.10(1) Å, corresponding to σ -bonded carbon atoms of neosilyl ligands, and one chloride at 2.41(1) Å. The W-C bond distance is in the same range as those found in the Me₃SiO-W(Ns)₃O moieties of the bimetallic complex [Me₃SiO-W(Ns)₃O-WN₃(≡CSiMe₃)] (2.084–2.106 Å for W-C)⁵⁷ while the W=O bond of these moieties (1.729–1.746 Å) is longer due to the bridging nature of the oxo ligand. The W=O bond distance in 1-Ns is, however, typically in the range found for similar complexes, as for [O(WONp₃)₂]⁵⁸ with W=O in the range 1.676–1.736 Å (W-C 2.113–2.150 Å), or for [OWCpNs₃]⁵⁹ (1.664(8) Å for W=O, W-C_{Ns} 2.231–2.322 Å). In addition, similar W-Cl bond distances have been observed in [W^{VI}OCIX₃] type complexes: 2.397 and 2.427 Å for (μ_2 -oxo)bis(benzoyltrifluoroacetonato)-dichlorooxotungsten(VI) (with a 1.696 Å W=O bond length)⁷¹ and 2.4212(2) Å for [WO(C₆H₁₂O₂)(C₆H₁₃O₂)Cl] (with a 1.716(3) Å W=O bond length).⁷² Similar parameters were obtained when fitting the $k^2\chi(k)$ spectrum. Furthermore, the fit was improved when considering a further layer of three Si atoms backscatterers at 3.43(3) Å, assigned to the Si of the neosilyl ligands. This corresponds to the distance found for the bimetallic complex [Me₃SiO-W(Ns)₃O-W(Ns)₃(≡CSiMe₃)] cited above, 3.423(6)–3.442(6) Å,⁵⁷ where [W-C-Si] angles from 118.9(2) to 119.1(3)[°] were found. The consideration of two multiple scattering O=W-Cl pathways also improved the fit, corresponding to a quasi-linear arrangement of these three atoms in the complex (trans configuration), as proposed by Osborn et al. for [WO-

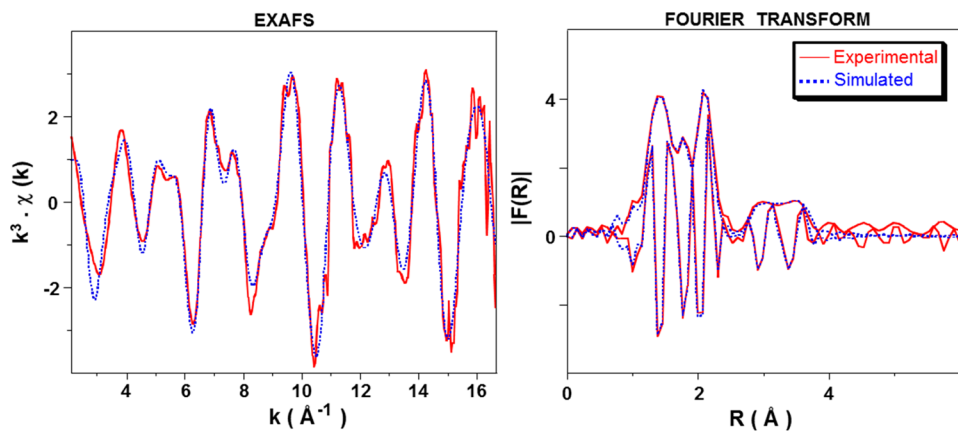


Figure 15. Tungsten L_{III}-edge k^3 -weighted EXAFS (left) and corresponding Fourier transform (right, modulus and imaginary part) with comparison to simulated curves for 1-Ns: (solid lines) experimental results; (dashed lines) spherical wave theory.

Table 2. EXAFS Parameters for Complex 1-Ns and DFT-Calculated Distances^a

type of neighbor	no. of neighbors	distance (Å)	DFT-calculated distance (Å)	σ^2 (Å ²)
W=O	1.0(2)	1.694(8)	1.703	0.0015(5)
W-CH ₂ SiMe ₃	3.0(4)	2.10(1)	2.100 ^d	0.0030(9)
W-Cl	1.0(6) ^b	2.41(1)	2.456	0.0022(6)
W-CH ₂ SiMe ₃	3	3.43(3)	3.464 ^e	0.011(5)
MS ₃₁ O=W-Cl ^c	2	4.07(4)		0.003(3)
MS ₄₁ O=W-Cl ^c	2	4.07 ^b		0.003 ^b

^aThe errors generated by the EXAFS fitting program “RoundMidnight” are indicated in parentheses. Δk (2.2–16.6 Å⁻¹) – ΔR (0.7–3.9 Å) ((0.7 – 2.5 Å), when considering only the first coordination sphere). $S_0^2 = 0.94$. $\Delta E_0 = 8.0 \pm 2.0$ eV (the same for all shells). Fit residue: $\rho = 6.4\%$. Quality factor: $(\Delta\chi)^2/\nu = 1.42$, with $\nu = 18/31$ ($(\Delta\chi)^2/\nu$)₁ = 2.93 with $\nu = 9/18$, considering only the first coordination sphere O, C, and Cl). ^bShell constrained to the parameters above. ^cThese two multiple scattering pathways (three and four legs) have been considered in the fit, assuming a geometry close to linearity between these three atoms. ^dAverage value for three W-C distances. ^eAverage value for three W-Si distances

(Np)₃Cl].⁵⁴ These experimental results are in excellent agreement with the DFT-calculated values.

Figure 16 displays the W L_{III}-EXAFS spectrum of the species resulting from the grafting of 1-Ns onto SiO₂₋₂₀₀, namely 2-Ns. The nearly complete disappearance of the direct W-Cl and multiple (O=W-Cl) scattering pathways can be clearly observed from the comparison of the moduli of the Fourier transforms of both molecular and supported species (contribution of the Cl backscatterer at ca. 2.1 Å and of the multiple scattering pathways at ca. 3.7 Å on the right part of Figure 16). The parameters extracted from the fit of the EXAFS spectrum (Table 3) agree with one oxo ligand at 1.693(6) Å, ca. two oxygen atoms at 1.86(1) Å and two carbon atoms at 2.11(1) Å, and ca. 0.1 chlorine at 2.40(1) Å respectively assigned to ca. two siloxide and two neosilyl ligands and very few residual chlorines, consistently with W=O, W-C, and W-Cl bond distances found in tungsten oxo complexes (see above) and with the two O-W bond distances in the range 1.852(2)–1.866(8) Å found in O=WN₂(Me₄pyde) (pyde = 2,6-pyridinediethanolate; 1.708(8)–1.711(9) Å for W=O and 2.204(12)–2.236(15) Å for W-C). The shorter W-O distance found for these ≡SiO-W moieties in comparison to that obtained for [≡SiO-WON₃] (1.98(2) Å)^{21,47,64} may indicate that the oxo and a siloxy ligand are not fully trans to each other in this surface complex, which may be slightly distorted in comparison to an ideal TBP geometry. Indeed, DFT calculations indicate that the tungsten species should exist both in trigonal-bipyramidal and square-pyramidal configura-

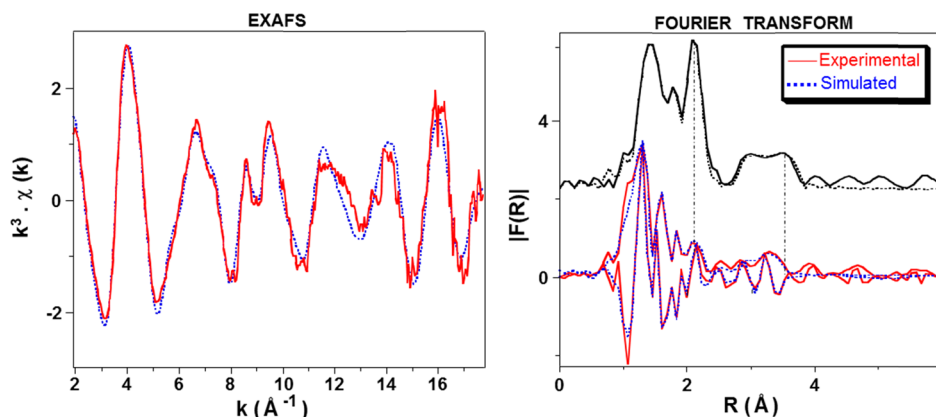


Figure 16. Tungsten L_{III}-edge k^3 -weighted EXAFS (left) of 2-Ns and corresponding Fourier transform (right; modulus and imaginary part, Fourier transform corresponding to complex 1-Ns for comparison shown in black), superimposed with simulated curves: (solid lines) experimental data; (dashed lines) spherical wave theory.

Table 3. EXAFS Parameters for the Supported Complex 2-Ns and DFT-Calculated Values^a

type of neighbor	no. of neighbors	distance (Å)	DFT-calculated distance (Å)		
			TBP geometry ^d	SP geometry ^e	σ^2 (Å ²)
W=O	1.0(1)	1.693(7)	1.712	1.692	0.0017(5)
W—OSi≡	2.1(2)	1.86(1)	1.93 ^f	1.928	0.0068(9)
W—CH ₂ SiMe ₃	1.8(2)	2.11(1)	2.098	2.140	0.0075(25)
W—Cl	0.1(5) ^b	2.40(1)			0.0025(9)
WCH ₂ SiMe ₃	1.8 ^b	3.51(3)	3.445	3.489	0.018(12)
W—OSi≡ ^c	2.1 ^b	3.51 ^b	3.515 ^f	3.407	0.0094(30)

^aThe errors generated by the EXAFS fitting program “RoundMidnight” are indicated in parentheses. Δk (1.9–17.7 Å⁻¹) – ΔR (0.6–3.9 Å) ((0.6–2.4 Å), when considering only the first coordination sphere). $S_0^2 = 0.94$. $\Delta E_0 = 6.9 \pm 1.0$ eV (the same for all shells). Fit residue: $\rho = 6.3\%$. Quality factor: $(\Delta\chi)^2/\nu = 2.07$, with $\nu = 18/35$ ($[(\Delta\chi)^2/\nu]_1 = 4.15$ with $\nu = 8/20$, considering only the first coordination sphere O, C, and Cl). ^bShell constrained to the parameters above. ^cTwo (W—O—Si) type multiple scattering pathways (three and four legs) have also been considered in the fit but are not mentioned in this table. ^dTrigonal-bipyramidal geometry, average values for both the ac and b model derived species 2^b-Ns_{bi} and 2^{ac}-Ns_{bi} (Table S1 in the Supporting Information). ^eSquare-pyramidal geometry, average values for both the ac and b model derived species 2^b-Ns_{bi} and 2^{ac}-Ns_{bi} (Table S1). ^fAverage value for the chemically distinct siloxide moieties, namely in positions cis and trans to the apical oxo ligand (see Table S1 for the individual distances).

tions, both of very close energetic levels. Most likely EXAFS-derived geometrical parameters may be the consequence of fast exchange between the two forms. Similar parameters were obtained when fitting the $k^2\chi(k)$ spectrum. The fit was also improved by adding two layers of silicon backscatterers, both at 3.51(3) Å, one composed of ca. two silicon atoms accounting for the quaternary silicons of the neosilyl ligands and another with ca. two silicon atoms from silicon atoms of surface siloxide ligands. These two layers were placed at the same distance from the W center in order to simplify the fit, and also because the resolution of the spectrum (about 0.09 Å) might be close to the difference between the distances of the two types of silicon from the tungsten center.

From these combined spectroscopic and analytical elements, and as hinted by the preliminary elements from Xue and co-workers, the reaction of 1-Ns with the silica surface dehydroxylated at 200 °C proceeds by W—Cl and W—CH₂SiMe₃ silanolysis and concomitant HCl and TMS release (Scheme 2). Comparatively, for the neopentyl derivative, the grafting stops at the W—Cl cleavage stage. By switching from neopentyl to neosilyl ligands, a clear difference in reactivity is thus observed, as initially expected. The neosilyl complex undergoes W—C protonolysis upon mild thermal treatment, affording the targeted bipodal tungsten oxo dineosilyl surface species. Such a small change (formally substituting a C atom for a Si in a β position from the metal center) induces a major difference in reactivity that is also reminiscent of previous results obtained on comparison of the reactivity of homoleptic species [M(CH₂R)₄] (M = Ti, Zr, R = CMe₃, Ph).⁶⁴ These examples further demonstrate the complexity of surface silica reactivity toward organometallic complexes: the choice of the organometallic precursor can indeed have a major impact on the resulting grafted species and, therefore, on the catalytic properties of the material.

Catalytic Performances in Olefin Metathesis. Catalytic performances of 2-Ns in propylene homocoupling were probed in a flow reactor (20 mL of C₃H₆ min⁻¹; 80 °C; 60 mol of C₃H₆ (mol of W)⁻¹ min⁻¹). A maximum conversion of 30% was reached after a fairly short induction period (about 2 h, due to the in situ formation of the active tungsten alkylidene surface species), and 24000 cumulated turnover numbers (TONs) were achieved after 25 h (Figure 17). The selectivity remained constant with time on stream, with equimolar quantities of ethylene and 2-butenes (no other alkene was detected; Figure

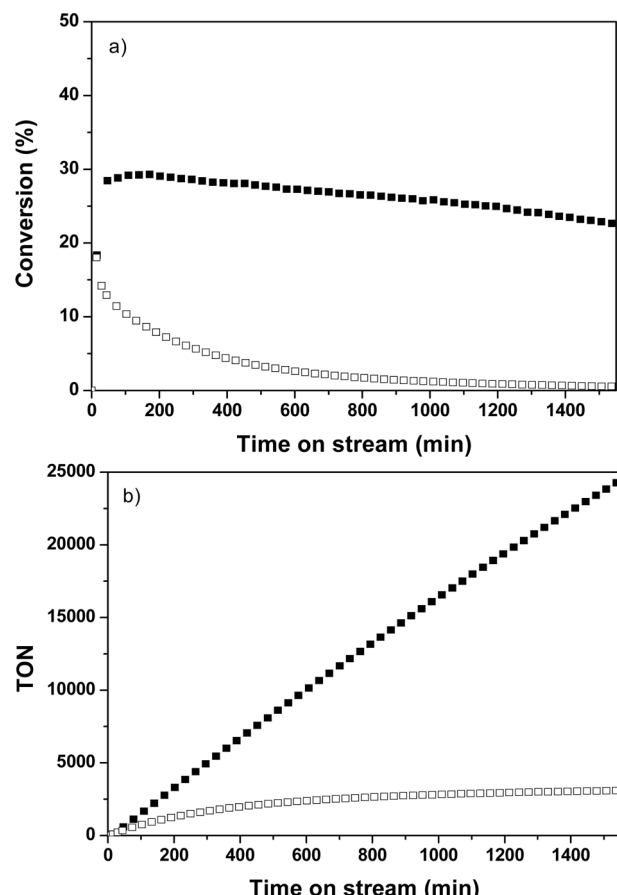


Figure 17. Conversion (a) and cumulated TON (b) of propylene self-metathesis (20 mL of C₃H₆ min⁻¹; 80 °C; 60 mol of C₃H₆ (mol of W)⁻¹ min⁻¹, 1 bar) over 2-Ns (■) and 2-OAr (□).

S7 in the Supporting Information). After the onset of the catalysis, the *trans*-/*cis*-2-butene selectivity kept to a constant value of 2.08 (thermal equivalent 2.3). Clearly, 2-Ns showed high stability under a continuous flow of propylene. Furthermore, no formation of polymeric products was observed (by solid-state NMR) after the end of the test. It should be noted that this catalyst is as stable but more active than the catalyst we obtained from a monosilox complex, (≡SiO)WONp₃, supported onto SiO₂₋₇₀₀, for which only 6000

cumulated TONs were achieved after 25 h.²¹ In addition, it has recently been reported that supported tungsten bearing bulky aryloxide as a spectator ligand is a heterogeneous metathesis catalyst.¹⁹ This catalyst comprised grafting of recently published organometallic tungsten oxo alkylidene complexes [WO(CHR)(dAdPO)₂] (R = tBu, CMe₂Ph)⁷³ by Schrock and co-workers on silica dehydroxylated at 700 °C, resulting in a monopodal tungsten oxo alkylidene surface species with an additional bulky aryloxide as spectator ligand. Although high TONs were reported for self-metathesis of selected liquid substrates in a batch reactor, the unlimited contact time between the catalyst and substrate does not reflect the real stability and robustness of the catalyst with time, especially when the time to equilibrium was between several minutes to a maximum of a few hours. In order to reveal the stability and robustness of the latter material with respect to **2-Ns** (being a supported bipodal tungsten oxo species active in olefin metathesis), [WO(CHtBu)(dAdPO)₂] has been prepared according to the published method⁷³ and grafted onto silica dehydroxylated at 700 °C, affording **2-OAr**.¹⁹ Surprisingly, when **2-OAr** was exposed to a continuous flow of propylene with a molar flow rate of 60 mol of C₃H₆ (mol of W)⁻¹ min⁻¹ (20 mL of C₃H₆ min⁻¹; 80 °C, 1 bar), a very fast deactivation was observed (Figure 17). Since **2-OAr** already contains the active tungsten alkylidene moiety, the initial activity was equal to the maximum conversion (18% conversion, comparable with **2-Ns**). However, **2-OAr** was practically inactive after 25 h, giving a final cumulated TON of about 3000.

Under the chosen conditions, **2-OAr** gave only metathesis products (ethylene, *trans*-2-butene, *cis*-2-butene) in equimolar quantities. No heavier alkenes were detected. The trans/cis ratio of 2-butene altered with time on stream: 1.93 at maximum conversion and converging toward 1.07 at the end of the test (Figure S8 in the Supporting Information). Similar evolution of the trans/cis ratio has already been observed for supported tungsten metathesis catalysts bearing an aryloxide.²⁹ Although **2-OAr** and **2-Ns** (after activation with the olefinic substrate) have the same coordination environment and both catalysts are active in propylene metathesis, there is a remarkable difference in stability, as revealed in a continuous flow reactor equipped with an online analytic tool. The local structure of **2-Ns** closely resembles the proposed industrial WO₃/SiO₂ catalyst and showed a fairly stable catalytic activity with time on stream of propylene. On the other hand, **2-OAr** belongs to a “model of a model” rather than being a true and robust catalyst and deactivated rapidly with time on stream. The huge difference in the catalytic performance may be due to the importance of the bipodal nature of **2-Ns**, or the presence of a bulky organic ligand in **2-OAr**, which can gradually undergo intramolecular C–H activation⁵⁰ with time and loss of the active tungsten alkylidene sites.

The fact that **2-Ns** is active in propylene self-metathesis showed that the necessary tungsten carbene moiety is generated *in situ* by α-H abstraction at gentle heating to 80 °C assisted by the substrate. A similar activation scheme has already been observed on supported tungsten methyl^{22,49} or hydride⁸ precatalysts for olefin metathesis reactions. In order to observe a reactive intermediate (whether carbenes or metallacyclobutanes), ¹³C-labeled ethylene (100% ¹³C, 40 equiv with respect to the total amount of tungsten) was reacted with **2-Ns** in a batch reactor for further solid-state ¹³C NMR studies. Unfortunately, no signal between 250 and 300 ppm, characteristic of a primary tungsten carbene moiety, was detected.

However, an intense peak centered at 32–34 ppm appeared (Figure S9 in the Supporting Information). The same signal has also been reported when **2-OAr** is exposed to ¹³C-enriched ethylene¹⁹ and has previously been assigned to the carbon atom within a supported oxo tungstacyclobutane intermediate exhibiting a square-based-pyramidal geometry, even though the expected peaks around 42 and 22 ppm were missing.⁷⁴ Interestingly, no reaction with isotopically labeled ethylene and the molecular precursor [WO(CHtBu)(dAdPO)₂] occurred in C₆D₆ due to the high degree of steric hindrance, as documented by Schrock and co-workers.⁷³ Only in the presence of Lewis acid, such as BArF, does ethylene insert into the tungsten carbene moiety. An example of isolated and stable tungsten oxo metallacyclobutane (with square-based-pyramidal geometry, characterized by elemental analysis, NMR, and X-ray diffraction) being closely related to this system is based on W(O)(CH-tBu)(OHMT)(OSi-tBu₃) (OHMT = 2,6-dimesitylphenoxide), where the CS of the metallacyclobutane carbon atoms appeared at 42 and 22 ppm in C₆D₆.⁷⁴ There is clearly a mismatch of the NMR data between the homogeneous model and **2-Ns**, as well as **2-OAr**, after contact with ¹³C-enriched ethylene. Nevertheless, it has been described that the metallacyclobutane of the W(O)(CH₂CH₂CH₂)(OHMT)₂ system can decompose to a tungsten hydride propenyl moiety.⁷³ The presence of tungsten hydride can easily polymerize the excess ethylene by multiple insertions, as reported in the direct conversion of ethylene to propylene.³⁹ Hence, **2-Ns** contacted with isotopically labeled ethylene has been subjected to DSC analysis in order to eventually reveal the formation of polyethylene. DSC showed a weak but rather clear endothermal signal at 124 °C, which corresponds to a polymeric material between low-density polyethylene and heavy polyethylene waxes (Figure S10 in the Supporting Information).⁷⁵ Thus, the signal in ¹³C CP MAS NMR (peak at 32–34 ppm) of **2-Ns** after reaction with isotopically labeled ethylene is assigned to polyethylene rather than to unsubstituted tungstacyclobutane species.

CONCLUSION

In the quest for a realistic model of the active species within the key industrial catalyst WO₃/SiO₂, we have succeeded in preparing an oxo bis-alkyl tungsten complex doubly anchored on the silica support. This species is closely related to the oxo alkylidene tungsten surface organometallic fragment postulated to account for olefin metathesis activity. This was accomplished by adjusting the nature of the alkyl ligand within the organometallic precursor, as hinted by previous work from Xue and co-workers: a switch from the neopentyl to neosilyl group allowed us to trigger the W–C activation and thus to generate the targeted bipodal structure through consecutive W–Cl and then W–C silanolysis on a mildly dehydroxylated support. The nature of the resulting surface species was demonstrated by mass balance analysis, elemental analysis, infrared, advanced (1D and 2D ¹H, ¹³C, ²⁹Si and ¹⁷O) solid-state NMR, and EXAFS. Furthermore, DFT calculations allowed us to understand and rationalize the experimental results regarding grafting selectivity. This material efficiently performs propene metathesis under relatively mild conditions (80 °C), with sustained activity over 24 h operating time, in contrast to other recently reported postulated model species that rapidly deactivate under our operating conditions. Our current efforts are targeted at the transformation of the bis-alkyl species into alkylidene centers or related species, which still

elude observation. This new strategy will be extended to the corresponding industrial catalyst based on supported molybdenum oxide on silica.

EXPERIMENTAL SECTION

All experiments were carried out by using standard Schlenk and glovebox techniques. Solvents were purified and dried according to standard procedures. C_6D_6 (SDS) was distilled from NaK and stored in a glovebox. $[WONp_3Cl]$, $[WO(CHtBu)(dAdPO)_2]$, and $[(\equiv SiO)WO(CHtBu)(dAdPO)]$ were synthesized following the literature procedures.^{19,47,73} Propene (Air Liquide, 99.5%) was dried and deoxygenated before use by passing it through freshly regenerated molecular sieves (3 Å) and R3-15 catalysts (BASF). ^{13}C -labelled ethylene (Eurisotop) was stored over freshly activated molecular sieves (3 Å) and R3-15 catalysts (BASF). SiO_{2-200} and SiO_{2-700} were prepared from Aerosil silica (Degussa, specific area of 200 $m^2 g^{-1}$), which was partly dehydroxylated at 200 and 700 °C, respectively, under high vacuum (10^{-5} Torr) for 15 h to give a white solid having a specific surface area of 190 $m^2 g^{-1}$ and containing 2.3 and 0.7 OH nm⁻², respectively. Gas-phase analyses were performed on a Hewlett-Packard 5890 series II gas chromatograph equipped with a flame ionization detector and an Al_2O_3/KCl on fused silica column (50 m × 0.32 mm). Elemental analyses were performed at the Pascher Mikroanalytisches Labor at Remagen-Bandorf, Germany. IR spectra were recorded on a Nicolet 6700 FT-IR spectrometer in either transmission or DRIFT mode in an airtight cell equipped with CaF_2 windows. The samples were prepared under argon within a glovebox. Typically, 64 scans were accumulated for each spectrum (resolution 4 cm⁻¹). ^{17}O -enriched complexes and silica surfaces were prepared using 90% ^{17}O -labeled water (Cortecnet) following procedures described below for complex 1-Ns or previously reported for silica.⁶⁷

NMR Characterization. Solution NMR spectra were recorded on an Avance-300 Bruker spectrometer. All chemical shifts were measured relative to residual 1H or ^{13}C resonances in the deuterated solvent: C_6D_6 , δ 7.15 ppm for 1H , 128 ppm for ^{13}C . 1H and ^{13}C solid-state NMR spectra were recorded on Bruker Avance-500 and Bruker Avance-300 spectrometers with a conventional double-resonance 4 mm CP MAS probe at the Laboratoire de Chimie Organométallique de Surface. The samples were introduced under argon in a zirconia rotor (4 mm), which was then tightly closed. The rotation frequency was set to 10 kHz unless otherwise specified. Chemical shifts were given with respect to TMS as external reference for 1H and ^{13}C NMR and to water for ^{17}O NMR. 1H and ^{17}O solid-state NMR spectra were acquired on a Bruker Avance III 800 (1H , 800.13 MHz; ^{17}O , 108.47 MHz) and 900 (^{17}O , 122.11 MHz) spectrometers. Two-dimensional (2D) 1H – 1H double quantum magic-angle spinning spectra were acquired at 20 kHz spinning speed using the R12₂⁵ symmetry-based recoupling scheme⁷⁶ applied for 200 μ s at an rf field strength of 40 kHz. The recycle delay was set to 2 s, and 16 transients were added for each of the 300 t_1 increments. The ^{17}O MAS NMR spectra at 18.8 and 21.15 T were acquired using a single pulse sequence (pulse excitation of 2 μ s at an rf field strength of 60 kHz) at spinning frequencies ranging from 17.6 to 20 kHz (3.2 mm rotor diameter) to avoid overlapping of spinning sidebands with CS resonances and to determine isotropic chemical shifts. No proton decoupling was applied. The recycle delay was 1 s. The ^{17}O MQMAS spectra were collected using the Z-filter sequence, which consists of two hard pulses of 4 and 1.8 μ s at

an rf field of 80 kHz for triple-quantum excitation and reconversion, respectively, followed by a soft pulse of 9 μ s at an rf field of 8 kHz. The t_1 step was set to the MAS period. A total of 6000 transients were added with a recycling delay of 0.8 s. The HMQC experiments were set up with a ^{17}O spin echo selective to the central transition, with pulses of 10 and 20 μ s. For the D-HMQC acquisition, the recoupling scheme (SR4) was applied for 1.2 ms. A total of 16384 transients were added with a recycling delay of 0.5 s.

Preparation and Characterization of $[W(OAr)_3Cl_3]$ (Ar = 2,6-Diisopropylphenyl). A solution of 2,6-diisopropylphenol (15 mL, 80.1 mmol) in 50 mL of toluene was added dropwise to a slurry of WCl_6 (10 g, 25.2 mmol) in 120 mL of toluene. The mixture was then heated to reflux for 16 h. Volatiles were removed under vacuum, leaving a black oil. After extensive drying the residue was washed five times with pentane to remove the excess phenol, leaving a black microcrystalline product (16.98 g, 82%) with spectroscopic features analogous to those previously reported.⁷⁷ $\delta(^1H, CD_2Cl_2)$: δ 6.7.29 (6 H, m, m-Ar), 6.98 (3 H, m, p-Ar), 4.06 (4 H, m, $CH(CH_3)_2$), 3.64 (2 H, m, $CH(CH_3)_2$), 1.12 (24 H, d, $CH(CH_3)_2$), 1.02 (12 H, d, $CH(CH_3)_2$).

Preparation and Characterization of $[W(\equiv CSiMe_3)-(CH_2SiMe_3)_3]$. A solution of $W(OAr)_3Cl_3$ (12 g, 14.6 mmol) in 100 mL of ether was added portion wise to a 0.5 M solution of $MgNsCl$ (180 mL, 0.89 mmol) in ether at 0 °C with rapid stirring. After 1 h the reaction mixture was warmed to room temperature and stirred for a further 16 h. Volatiles were then removed under vacuum, and the solid was extracted three times with 80 mL of pentane and filtered through Celite. Volatiles were removed under vacuum, and the dark residue was sublimed at 90 °C under high vacuum (10^{-5} Torr), giving 5.05 g (65%) of yellow product with spectroscopic features analogous to those previously reported.⁷⁸ $\delta(^1H, C_6D_6)$: δ 0.71 (6 H, s, CH_2SiMe_3 , $^2J_{WH} = 10.1$ Hz, $^2J_{SiH} = 8.2$ Hz), 0.42 (9 H, s, $\equiv CSiMe_3$, $^2J_{SiH} = 6.6$ Hz), 0.16 (27 H, s, CH_2SiMe_3 , $^2J_{SiH} = 6.5$ Hz). $\delta(^{13}C\{^1H\}, C_6D_6)$: 343.6 (s, $\equiv CSiMe_3$, $J_{WH} = 171.8$ Hz), 75.90 (s, CH_2SiMe_3 , $^2J_{WH} = 79.0$ Hz, $^2J_{SiH} = 42.0$ Hz), 2.40 (s, CH_2SiMe_3 , $^2J_{WH} = 51.4$ Hz, $^2J_{SiH} = 23.0$ Hz), 2.22 (s, $\equiv CSiMe_3$, $^2J_{WH} = 52.6$ Hz, $^2J_{SiH} = 24.9$ Hz). $\delta(^{29}Si\{^1H\}, C_6D_6)$: -1.34 (s, CH_2SiMe_3), -18.06 (s, $\equiv CSiMe_3$).

Preparation and Characterization of $[WO(CH_2SiMe_3)_3Cl]$ (1-Ns). Two equivalents of H_2O (81 μ L, 4.522 mmol) in 45 mL of THF was added dropwise at -78 °C to a vigorously stirred solution of $[W(\equiv CSiMe_3)-(CH_2SiMe_3)_3]$ (1.2 g, 2.261 mmol) in 50 mL of THF. The temperature was slowly raised to -40 °C, at which point the solution turned red. After 30 min the solution was then warmed to room temperature. Then 2 equiv of Me_3SiCl (0.57 mL, 4.522 mmol) was added to the reaction mixture. An immediate color change from reddish orange to yellow was observed upon addition of the Me_3SiCl . The solvent was then removed under vacuum to leave a pale solid. The crude material was sublimed at 80 °C under reduced pressure (10^{-5} mbar) to yield 0.78 g of pure white product (70% yield). Anal. Calcd. for $C_{12}H_{33}ClOSi_3W$: C, 29.00; H, 6.69; C, 28.78; H, 6.82. $\delta(^1H, C_6D_6)$: 2.29 (6 H, s, WCH_2 , $^2J_{WH} = 11.0$ Hz), 0.20 (27 H, s, $Si(CH_3)_3$). $\delta(^{13}C\{^1H\}, C_6D_6)$: 76.13 (WCH_2 , $^1J_{WC} = 85.1$ Hz), 1.95 ($Si(CH_3)_3$). $\delta(^{29}Si, C_6D_6)$: 0.9 ($CH_2Si(CH_3)_3$).

Preparation and Characterization of 2-Np. A mixture of 1-Np (150 mg, 0.33 mmol) and SiO_{2-200} (1 g) was stirred at 25 °C under dynamic vacuum while all volatile compounds were condensed into a cold trap. Pentane was then added, and the

solid was washed five times. The resulting white powder was dried under vacuum (10^{-5} Torr). Analysis by infrared spectroscopy of the condensed volatiles indicated the formation of 240 μmol of HCl during the grafting (0.9 HCl/W). The solid was then heated at 80 °C for 4 h, and analysis by gas chromatography indicated the formation of 0.1 neopentane per tungsten. Anal. Found: W, 4.34; C, 4.08; H, 0.83. ^1H MAS solid-state NMR (800 MHz): δ 2.1, 1.2 ppm. ^{13}C CP/MAS solid state NMR (200 MHz): δ 91, 35, and 31 ppm.

Preparation and Characterization of 2-Ns. A mixture of finely ground 1-Ns (230 mg, 0.462 mmol) and SiO_{2-200} (600 mg) was stirred at 80 °C (5 h) under dynamic vacuum while all volatile compounds were condensed into a cold trap. Pentane was then added, and the solid was washed five times. The resulting yellow powder was dried under vacuum (10^{-5} Torr) and transferred to a 500 mL Schlenk tube in order to quantify tetramethylsilane evolved during grafting. The powder was then heated at 70 °C under static vacuum for 24 h. Anal. Found: W, 5.72; C, 3.35; H, 0.51. ^1H MAS NMR (500 MHz): δ 0.5 and 1.8 ppm. ^{13}C CP MAS NMR (125 MHz): δ 65.68 and 0.5 ppm. ^{29}Si CP MAS NMR (MHz): δ 2.18 ppm.

Procedure for the Quantification of HCl and TMS Released during Grafting. The gas phase released during grafting was condensed into an IR cell equipped with CaF_2 windows. Transmission infrared spectra were recorded on a Nicolet 5700 FT spectrometer, at room temperature. The resolution was 1 cm^{-1} with 16 scans. HCl was quantified by comparison of the surface of the absorbance IR bands in the 2600–3100 cm^{-1} region of the sample to a calibration curve. For the calibration, known amounts of pure HCl were introduced into the same gas cell and IR spectra were recorded.

A mixture of finely ground 1-Ns (192 mg, 0.385 mmol) and SiO_{2-200} (500 mg) was stirred at 25 °C (2 h) under dynamic vacuum while all volatile HCl was removed. No TMS was released at this stage.⁴⁷ The resulting white powder was heated at 80 °C and became yellow after 3 h. TMS evolved was transferred to a 100 mL Schlenk tube and thereafter condensed in an NMR tube containing FeCp_2 (29 mg, 0.1556 mmol) as an internal standard dissolved in C_6D_6 .

Propene Metathesis. The evaluation of the activity of the catalysts in propene metathesis has been performed in a 1/2 in. stainless steel continuous flow reactor. The catalytic tests were performed at 80 °C, with a propylene flow rate fixed at 20 mL min^{-1} and molar flow rate of 60 mol of C_3H_6 (mol of W) $^{-1}$ min^{-1} . The products were analyzed by online GC (HP 6890) equipped with a $\text{KCl}/\text{Al}_2\text{O}_3$ column and FID. The conversion and selectivity were calculated from carbon numbers directly from GC. Cumulated TONs were calculated by assuming that the total amount of tungsten is active. The carbon balance was constant during the catalytic tests, according to the online GC.

DSC Analysis. These measurements were performed in a Mettler Toledo DSC 1 instrument, equipped with an autosampler. The temperature and the heat flow of the equipment were calibrated with an indium standard. The sample was accurately weighed and heated from 40 to 180 °C at 10 °C min^{-1} with an empty aluminum pan as reference. Two successive heating and cooling cycles were performed, and only the second run was considered. Dry nitrogen with a flow rate set at 30 mL min^{-1} was used as the purge gas. The melting temperature (T_m) was measured at the top of the endothermic peak. The STARe thermal analysis software was used for the calculation.

SIMPSON Simulation of ^{17}O MAS NMR Spectra. All ^{17}O MAS NMR numerical spectra were calculated using the *gcompute* method implemented in the SIMPSON software package.⁷⁹ This package described each line shape with nine NMR interaction parameters, which included the isotropic chemical shift (δ_{CS}) defined in eq 1, the quadrupole coupling constant (C_Q) and quadrupole asymmetry parameter (η_Q) defined in eqs 2 and 3, the CSA (Δ_{CSA}) and chemical shift asymmetry parameter (η_{CSA}) (in the Haeberlen convention) defined in eqs 4 and 5, and the Euler angles (α, β, γ). Here the Euler angles were kept to 0 due to the impossibility of assessing them with the available experimental data sets. Each numerical simulation was performed with the zcw4180 crystallite file and 30 γ angles, with the calculated FID inclusive of all quadrupolar satellites. Line broadenings of 500 and 1500 Hz were applied for simulated spectra of 2-Np-O* and 2-Ns-O* and of 2-Np-SiO₂* and 2-Ns-SiO₂*, respectively, with a Gaussian/Lorentzian ratio of 0.8.

$$\delta_{\text{CS}} = (\delta_{11} + \delta_{22} + \delta_{33})/3 \quad (1)$$

$$C_Q = e^2 q Q/h = e V_{33} Q/h \quad |V_{33}| \geq |V_{22}| \geq |V_{11}| \quad (2)$$

$$\eta_Q = (V_{11} - V_{22})/V_{33} \quad 1 \geq \eta_Q \geq 0 \quad (3)$$

$$\Delta_{\text{CSA}} = \delta_{zz} - (\delta_{xx} + \delta_{yy})/2 = 3\delta/2$$

$$|\delta_{zz} - \delta_{\text{CS}}| \geq |\delta_{xx} - \delta_{\text{CS}}| \geq |\delta_{yy} - \delta_{\text{CS}}| \quad (4)$$

with the reduced anisotropy $\delta = \delta_{33} - \delta_{\text{CS}}$

$$\eta_{\text{CSA}} = (\delta_{yy} - \delta_{xx})/(\delta_{zz} - \delta_{\text{CS}}) \quad 1 \geq \eta_{\text{CSA}} \geq 0 \quad (5)$$

DFT Methodological Details. All DFT calculations were performed with Gaussian 03.⁸⁰ Calculations were carried out at the DFT level of theory using the hybrid functional B3PW91.^{81–86} Geometry optimizations were achieved without any symmetry restriction. Calculations of vibrational frequencies were systematically done in order to characterize the nature of stationary points. Gibbs free energies were obtained at $P = 1$ atm and $T = 298.15$ K within the harmonic approximation for frequencies. Stuttgart effective core potentials and their associated basis sets were used for silicon and tungsten.⁸⁷ The basis sets were augmented by a set of polarization functions ($\zeta_d = 0.284$ for Si and $\zeta_f = 0.823$ for W). Hydrogen, chlorine, carbon, and oxygen atoms were treated with 6-31G(d,p) double- ζ basis sets.^{88,89} The optimized structures were used for ^{17}O NMR calculations. These calculations were also performed using the higher Dunning correlation consistent basis set cc-PVTZ for the oxygen atoms.^{90,91} In all cases, among the various theories available to compute chemical shielding tensors, the gauge including atomic orbital (GIAO) method was adopted for the numerous advantages it presents.^{92–97} Typically, in order to compare our calculations with experimental values, ^{17}O chemical shielding was converted to chemical shift using the usual equation: $\delta_{\text{iso}} = \sigma_{\text{iso}}(\text{ref}) - \sigma_{\text{iso}}(\text{sample})$, where $\sigma_{\text{iso}}(\text{ref})$ is the isotropic ^{17}O chemical shielding of the liquid water. In a continuation of our previous studies,⁴⁷ an internal reference was used for the calibration of the $\sigma_{\text{iso}}(\text{ref})$ value: $\sigma_{\text{iso}}(\text{ref}) = 292.2$ ppm. The ^{17}O quadrupolar coupling constant C_Q and the asymmetry parameter η_Q which describes the interaction between nuclear quadrupolar moment of the oxygen nuclei with the electric field gradient (EFG) arisen at these sites, were calculated from the EFG tensor

eigenvalues V_{11} , V_{22} , and V_{33} . It is now well-established that DFT methods are the computational method of choice to deal with coordination, reactivity, and property calculations, and this computational approach has proven its efficiency in guiding experimental analysis. In this study, both chemical and computational models were already validated in several previous studies.^{48,49,59–64,67} Table S6 in the Supporting Information compares Gibbs free energy values at 298 and 353 K of the grafting reactions of **1-Ns** and **1-Np** onto ac and b SiO₂₋₂₀₀ surface models.

EXAFS. X-ray absorption spectra were acquired at the ESRF, using the Swiss–Norwegian beamline BM01B (proposal no. 01-01-905), at room temperature at the tungsten L_{III} edge, with a double-crystal Si(111) monochromator detuned by 70% to reduce the higher harmonics of the beam. The spectra were recorded in the transmission mode between 9.98 and 11.45 keV. The supported W sample was packaged within an argon-filled glovebox in a double-airtight sample holder equipped with Kapton windows. The spectra analyzed were the results of four such acquisitions, and no evolution was observed between the first and last acquisitions. The data analyses were performed by standard procedures, using in particular the program Athena⁹⁸ and the EXAFS fitting program RoundMidnight,⁹⁹ from the MAX package, using spherical waves. The program FEFF8 was used to calculate theoretical files for phases and amplitudes on the basis of model clusters of atoms.¹⁰⁰ The value of the scale factor, $S_0^2 = 0.94$, was determined from the k^2 and $k^3 \cdot \chi(k)$ spectra of a reference compound, a sample of [WO-(CH₂fBu)₃Cl] complex (**1-Np**) diluted in BN and carefully mixed and pressed as a pellet (one oxo at 1.70(1) Å, three carbon atoms at 2.10(1) Å, and one chlorine at 2.43(1) Å in the first coordination sphere, with three carbon atoms at 3.28(3) Å).⁴⁷ The refinements were performed by fitting the structural parameters N_i , R_i , and σ_i and the energy shift ΔE_0 (the same for all shells). The fit residue, ρ (%), was calculated by the formula

$$\rho = \frac{\sum_k [k^3 \cdot \chi_{\text{exp}}(k) - k^3 \cdot \chi_{\text{cal}}(k)]^2}{\sum_k [k^3 \cdot \chi_{\text{exp}}(k)]^2} \times 100$$

As recommended by the Standards and Criteria Committee of the International XAFS Society, the quality factor, $(\Delta\chi)^2/\nu$, where ν is the number of degrees of freedom in the signal, was calculated and its minimization considered in order to control the number of variable parameters in the fits.

ASSOCIATED CONTENT

Supporting Information

The Supporting Information is available free of charge on the ACS Publications website at DOI: [10.1021/acscatal.5b01744](https://doi.org/10.1021/acscatal.5b01744).

Additional spectroscopic data, DFT calculations on the mechanistic aspects of the grafting reaction and on NMR parameters, and coordinates of DFT optimized structures (PDF)

AUTHOR INFORMATION

Corresponding Authors

*E-mail for L.M.: laurent.maron@irsamc.ups-tlse.fr.

*E-mail for L.D.: laurent.delevoye@ensc-lille.fr.

*E-mail for M.T.: mostafa.taoufik@univ-lyon1.fr.

Notes

The authors declare no competing financial interest.

ACKNOWLEDGMENTS

We thank Hermann Emerich for his help during the recording of the XAS spectra on the Swiss–Norwegian beamline BM01B at the ESRF (proposal no. 01-01-905). We thank a reviewer for an interesting suggestion. This work was principally financed by the Agence Nationale de la Recherche (ANR-12-BS07-0021-01, OXOCAT). The CNRS, French Ministry of Research and Higher Education, Institut de chimie de Lyon, Chevreul Institute (FR 2638), Région Nord–Pas de Calais, and FEDER are acknowledged for their supplementary support. Financial support from the TGE RMN THC Fr3050 for conducting the high-field solid-state NMR is gratefully acknowledged.

REFERENCES

- (1) Mudu, F.; Arstad, B.; Bakken, E.; Fjellvåg, H.; Olsbye, U. *J. Catal.* **2010**, *275*, 25–33.
- (2) Yang, J.; Ma, W. P.; Chen, D.; Holmen, A.; Davis, B. H. *Appl. Catal., A* **2014**, *470*, 250–260.
- (3) Bhasin, M. M.; McCain, J. H.; Vora, B. V.; Imai, T.; Pujado, P. R. *Appl. Catal., A* **2001**, *221*, 397–419.
- (4) Usman, M.; Daud, W. *RSC Adv.* **2015**, *5*, 21945–21972.
- (5) Bjørgen, M.; Joensen, F.; Holm, M. S.; Olsbye, U.; Lillerud, K. P.; Svelle, S. *Appl. Catal., A* **2008**, *345*, 43–50.
- (6) McCann, D. M.; Lesthaeghe, D.; Kletnieks, P. W.; Guenther, D. R.; Hayman, M. J.; Van Speybroeck, V.; Waroquier, M.; Haw, J. F. *Angew. Chem., Int. Ed.* **2008**, *47*, 5179–5182.
- (7) Tisse, V. F.; Boisson, C.; McKenna, T. F. L. *Macromol. Chem. Phys.* **2014**, *215*, 1358–1369.
- (8) Popoff, N.; Mazoyer, E.; Pelletier, J.; Gauvin, R. M.; Taoufik, M. *Chem. Soc. Rev.* **2013**, *42*, 9035–9054.
- (9) Balcar, H.; Cejka, J. *Coord. Chem. Rev.* **2013**, *257*, 3107–3124.
- (10) Lwin, S.; Wachs, I. E. *ACS Catal.* **2014**, *4*, 2505–2520.
- (11) van Schalkwyk, C.; Spamer, A.; Moodley, D. J.; Dube, T.; Reynhardt, J.; Botha, J. M. *Appl. Catal., A* **2003**, *255*, 121–131.
- (12) Bhuiyan, T. I.; Arudra, P.; Akhtar, M. N.; Aitani, A. M.; Abudawoud, R. H.; Al-Yami, M. A.; Al-Khattaf, S. S. *Appl. Catal., A* **2013**, *467*, 224–234.
- (13) Debecker, D. P.; Stoyanova, M.; Rodemerck, U.; Colbeau-Justin, F.; Boissiere, C.; Chaumonnot, A.; Bonduelle, A.; Sanchez, C. *Appl. Catal., A* **2014**, *470*, 458–466.
- (14) Hu, J. C.; Wang, Y. D.; Chen, L. F.; Richards, R.; Yang, W. M.; Liu, Z. C.; Xu, W. *Microporous Mesoporous Mater.* **2006**, *93*, 158–163.
- (15) Maksasithorn, S.; Debecker, D. P.; Praserthdam, P.; Panpranot, J.; Suriye, K.; Ayudhya, S. K. N. *Chin. J. Catal.* **2014**, *35*, 232–241.
- (16) Maksasithorn, S.; Praserthdam, P.; Suriye, K.; Devillers, M.; Debecker, D. P. *Appl. Catal., A* **2014**, *488*, 200–207.
- (17) Wang, Y. D.; Chen, Q. L.; Yang, W. M.; Xie, Z. K.; Xu, X.; Huang, D. *Appl. Catal., A* **2003**, *250*, 25–37.
- (18) Grunert, W.; Feldhaus, R.; Anders, K.; Shapiro, E. S.; Minachev, K. M. *J. Catal.* **1989**, *120*, 444–456.
- (19) Conley, M. P.; Forrest, W. P.; Mougel, V.; Coperet, C.; Schrock, R. R. *Angew. Chem., Int. Ed.* **2014**, *53*, 14221–14224.
- (20) Basset, J.-M.; Psaro, R.; Roberto, D.; Ugo, R. *Modern Surface Organometallic Chemistry*; Wiley-VCH: Weinheim, Germany, 2009.
- (21) Mazoyer, E.; Merle, N.; de Mallmann, A.; Basset, J. M.; Berrier, E.; Delevoye, L.; Paul, J. F.; Nicholas, C. P.; Gauvin, R. M.; Taoufik, M. *Chem. Commun.* **2010**, *46*, 8944–8946.
- (22) Bouhoute, Y.; Garron, A.; Grekov, D.; Merle, N.; Szeto, K. C.; De Mallmann, A.; Del Rosal, I.; Maron, L.; Girard, G.; Gauvin, R. M.; Delevoye, L.; Taoufik, M. *ACS Catal.* **2014**, *4*, 4232–4241.
- (23) Espinas, J.; Pelletier, J.; Szeto, K. C.; Merle, N.; Le Roux, E.; Lucas, C.; De Mallmann, A.; Basset, J. M.; Taoufik, M.; Thivolle-Cazat, J. *Microporous Mesoporous Mater.* **2014**, *188*, 77–85.
- (24) Garron, A.; Stoffelbach, F.; Merle, N.; Szeto, K. C.; Thivolle-Cazat, J.; Basset, J. M.; Norsic, S.; Taoufik, M. *Catal. Sci. Technol.* **2012**, *2*, 2453–2455.

- (25) Mazoyer, E.; Szeto, K. C.; Basset, J. M.; Nicholas, C. P.; Taoufik, M. *Chem. Commun.* **2012**, *48*, 3611–3613.
- (26) Mazoyer, E.; Szeto, K. C.; Merle, N.; Norsic, S.; Boyron, O.; Basset, J. M.; Taoufik, M.; Nicholas, C. P. *J. Catal.* **2013**, *301*, 1–7.
- (27) Mazoyer, E.; Szeto, K. C.; Norsic, S.; Garron, A.; Basset, J. M.; Nicholas, C. P.; Taoufik, M. *ACS Catal.* **2011**, *1*, 1643–1646.
- (28) Popoff, N.; Espinas, J.; Pelletier, J.; Szeto, K. C.; Thivolle-Cazat, J.; Delevoye, L.; Gauvin, R. M.; Taoufik, M. *ChemCatChem* **2013**, *5*, 1971–1977.
- (29) Popoff, N.; Szeto, K. C.; Merle, N.; Espinas, J.; Pelletier, J.; Lefebvre, F.; Thivolle-Cazat, J.; Delevoye, L.; De Mallmann, A.; Gauvin, R. M.; Taoufik, M. *Catal. Today* **2014**, *235*, 41–48.
- (30) Szeto, K. C.; Mazoyer, E.; Merle, N.; Norsic, S.; Basset, J. M.; Nicholas, C. P.; Taoufik, M. *ACS Catal.* **2013**, *3*, 2162–2168.
- (31) Szeto, K. C.; Hardou, L.; Merle, N.; Basset, J. M.; Thivolle-Cazat, J.; Papaioannou, C.; Taoufik, M. *Catal. Sci. Technol.* **2012**, *2*, 1336–1339.
- (32) Merle, N.; Taoufik, M.; Nayer, M.; Baudouin, A.; Le Roux, E.; Gauvin, R. M.; Lefebvre, F.; Thivolle-Cazat, J.; Basset, J. M. *J. Organomet. Chem.* **2008**, *693*, 1733–1737.
- (33) Genelot, M.; Cheval, N. P.; Vitorino, M.; Berrier, E.; Weibel, J.-M.; Pale, P.; Mortreux, A.; Gauvin, R. M. *Chem. Sci.* **2013**, *4*, 2680–2685.
- (34) Szeto, K. C.; Loges, B.; Merle, N.; Popoff, N.; Quadrelli, A.; Jia, H. P.; Berrier, E.; De Mallmann, A.; Delevoye, L.; Gauvin, R. M.; Taoufik, M. *Organometallics* **2013**, *32*, 6452–6460.
- (35) Norsic, S.; Larabi, C.; Delgado, M.; Garron, A.; de Mallmann, A.; Santini, C.; Szeto, K. C.; Basset, J. M.; Taoufik, M. *Catal. Sci. Technol.* **2012**, *2*, 215–219.
- (36) Szeto, K. C.; Merle, N.; Rios, C.; Rouge, P.; Llop Castelbou, J.; Taoufik, M. *Catal. Sci. Technol.* **2015**, *5*, 4765–4771.
- (37) Chen, Y.; Callens, E.; Abou-Hamad, E.; Merle, N.; White, A. J. P.; Taoufik, M.; Coperet, C.; Le Roux, E.; Basset, J. M. *Angew. Chem., Int. Ed.* **2012**, *51*, 11886–11889.
- (38) Popoff, N.; Macqueron, B.; Sayhoun, W.; Espinas, J.; Pelletier, J.; Boyron, O.; Boisson, C.; Merle, N.; Szeto, K. C.; Gauvin, R. M.; De Mallmann, A.; Taoufik, M. *Eur. J. Inorg. Chem.* **2014**, *2014*, 888–895.
- (39) Mazoyer, E.; Szeto, K. C.; Merle, N.; Thivolle-Cazat, J.; Boyron, O.; Basset, J. M.; Nicholas, C. P.; Taoufik, M. *J. Mol. Catal. A: Chem.* **2014**, *385*, 125–132.
- (40) Schrock, R. R. *Chem. Rev.* **2009**, *109*, 3211–3226.
- (41) Schrock, R. R.; Hoveyda, A. H. *Angew. Chem., Int. Ed.* **2003**, *42*, 4592–4633.
- (42) Coperet, C. *Dalton Trans.* **2007**, 5498–5504.
- (43) Wolke, S. I.; Buffon, R. *J. Mol. Catal. A: Chem.* **2000**, *160*, 181–187.
- (44) Rhers, B.; Salameh, A.; Baudouin, A.; Quadrelli, E. A.; Taoufik, M.; Coperet, C.; Lefebvre, F.; Basset, J. M.; Solans-Monfort, X.; Eisenstein, O.; Lukens, W. W.; Lopez, L. P. H.; Sinha, A.; Schrock, R. R. *Organometallics* **2006**, *25*, 3554–3557.
- (45) Balcar, H.; Zilkova, N.; Sedlacek, J.; Zednik, J. *J. Mol. Catal. A: Chem.* **2005**, *232*, 53–58.
- (46) Yuan, J.; Townsend, E. M.; Schrock, R. R.; Goldman, A. S.; Muller, P.; Takase, M. K. *Adv. Synth. Catal.* **2011**, *353*, 1985–1992.
- (47) Merle, N.; Girard, G.; Popoff, N.; De Mallmann, A.; Bouhouste, Y.; Trebosc, J.; Berrier, E.; Paul, J. F.; Nicholas, C. P.; Del Rosal, I.; Maron, L.; Gauvin, R. M.; Delevoye, L.; Taoufik, M. *Inorg. Chem.* **2013**, *52*, 10119–10130.
- (48) Solans-Monfort, X.; Coperet, C.; Eisenstein, O. *Organometallics* **2012**, *31*, 6812–6822.
- (49) Hamieh, A.; Chen, Y.; Abdel-Azeim, S.; Abou-hamad, E.; Goh, S.; Samantaray, M.; Dey, R.; Cavallo, L.; Basset, J. M. *ACS Catal.* **2015**, *5*, 2164–2171.
- (50) Couturier, J. L.; Paillet, C.; Leconte, M.; Basset, J. M.; Weiss, K. *Angew. Chem., Int. Ed. Engl.* **1992**, *31*, 628–631.
- (51) Mania, P.; Conrad, S.; Verel, R.; Hammond, C.; Hermans, I. *Dalton Trans.* **2013**, *42*, 12725–12732.
- (52) Bini, F.; Rosier, C.; Saint-Arroman, R. P.; Neumann, E.; Dablemont, C.; de Mallmann, A.; Lefebvre, F.; Niccolai, G. P.; Basset, J. M.; Crocker, M.; Buijink, J. K. *Organometallics* **2006**, *25*, 3743–3760.
- (53) Scott, S. L.; Fu, A. Q.; MacAdams, L. A. *Inorg. Chim. Acta* **2008**, *361*, 3315–3321.
- (54) Kress, J. R. M.; Russell, M. J. M.; Wesolek, M. G.; Osborn, J. A. *J. Chem. Soc., Chem. Commun.* **1980**, 431–432.
- (55) Feinstein-Jaffe, I.; Gibson, D.; Lippard, S. J.; Schrock, R. R.; Spool, A. *J. Am. Chem. Soc.* **1984**, *106*, 6305–6310.
- (56) Feinstein-Jaffe, I.; Pedersen, S. F.; Schrock, R. R. *J. Am. Chem. Soc.* **1983**, *105*, 7176–7177.
- (57) Morton, L. A.; Miao, M.; Callaway, T. M.; Chen, T.; Chen, S.-J.; Tuinman, A. A.; Yu, X.; Lu, Z.; Xue, Z.-L. *Chem. Commun.* **2013**, *49*, 9555–9557.
- (58) Sawant, D. P.; Vinu, A.; Mirajkar, S. P.; Lefebvre, F.; Ariga, K.; Anandan, S.; Mori, T.; Nishimura, C.; Halligudi, S. B. *J. Mol. Catal. A: Chem.* **2007**, *271*, 46–56.
- (59) Del Rosal, I.; Gerber, I.; Poteau, R.; Maron, L. *New J. Chem.* **2015**, *39*, 7703.
- (60) Del Rosal, I.; Gerber, I. C.; Poteau, R.; Maron, L. *J. Phys. Chem. A* **2010**, *114*, 6322–6330.
- (61) Del Rosal, I.; Poteau, R.; Maron, L. *Dalton Trans.* **2011**, *40*, 11211–11227.
- (62) Del Rosal, I.; Poteau, R.; Maron, L. *Dalton Trans.* **2011**, *40*, 11228–11240.
- (63) Del Rosal, I.; Tschan, M. J. L.; Gauvin, R. M.; Maron, L.; Thomas, C. M. *Polym. Chem.* **2012**, *3*, 1730–1739.
- (64) Popoff, N.; Espinas, J.; Pelletier, J.; Macqueron, B.; Szeto, K. C.; Boyron, O.; Boisson, C.; Del Rosal, I.; Maron, L.; De Mallmann, A.; Gauvin, R. M.; Taoufik, M. *Chem. - Eur. J.* **2013**, *19*, 964–973.
- (65) Schultz, N. E.; Zhao, Y.; Truhlar, D. G. *J. Comput. Chem.* **2008**, *29*, 185–189.
- (66) Zhao, Y.; Truhlar, D. G. *Acc. Chem. Res.* **2008**, *41*, 157–167.
- (67) Merle, N.; Trebosc, J.; Baudouin, A.; Del Rosal, I.; Maron, L.; Szeto, K.; Genelot, M.; Mortreux, A.; Taoufik, M.; Delevoye, L.; Gauvin, R. M. *J. Am. Chem. Soc.* **2012**, *134*, 9263–9275.
- (68) Czjzek, G.; Fink, J.; Gotz, F.; Schmidt, H.; Coey, J. M. D.; Rebouillat, J. P.; Lienard, A. *Phys. Rev. B: Condens. Matter Mater. Phys.* **1981**, *23*, 2513–2530.
- (69) Le Caer, G.; Brand, R. A. *J. Phys.: Condens. Matter* **1998**, *10*, 10715–10774.
- (70) Legzdins, P.; Rettig, S. J.; Sanchez, L. *Organometallics* **1985**, *4*, 1470–1471.
- (71) Sergienko, V. S.; Kovalenko, Y. V.; Ilyukhin, A. B.; Abramenco, V. L. *Zh. Neorg. Khim.* **1994**, *39*, 1320–1327.
- (72) Lehtonen, A.; Sillanpää, R. *Acta Crystallogr., Sect. C: Cryst. Struct. Commun.* **1998**, *54*, 935–937.
- (73) Peryshkov, D. V.; Forrest, W. P.; Schrock, R. R.; Smith, S. J.; Mueller, P. *Organometallics* **2013**, *32*, 5256–5259.
- (74) Peryshkov, D. V.; Schrock, R. R. *Organometallics* **2012**, *31*, 7278–7286.
- (75) Chen, Y.; Zou, H.; Liang, M.; Liu, P. *J. Appl. Polym. Sci.* **2013**, *129*, 945–953.
- (76) Carravetta, M.; Eden, M.; Zhao, X.; Brinkmann, A.; Levitt, M. H. *Chem. Phys. Lett.* **2000**, *321*, 205–215.
- (77) Quignard, F.; Leconte, M.; Basset, J. M.; Hsu, L. Y.; Alexander, J. J.; Shore, S. G. *Inorg. Chem.* **1987**, *26*, 4272–4277.
- (78) Andersen, R. A.; Chisholm, M. H.; Gibson, J. F.; Reichert, W. W.; Rothwell, I. P.; Wilkinson, G. *Inorg. Chem.* **1981**, *20*, 3934–3936.
- (79) Bak, M.; Rasmussen, J. T.; Nielsen, N. C. *J. Magn. Reson.* **2000**, *147*, 296–330.
- (80) Frisch, M. J.; Trucks, G. W.; Schlegel, H. B.; Scuseria, G. E.; Robb, M. A.; Cheeseman, J. R.; Montgomery, J. A., Jr.; Vreven, T.; Kudin, K. N.; Burant, J. C.; Millam, J. M.; Iyengar, S. S.; Tomasi, J.; Barone, V.; Mennucci, B.; Cossi, M.; Scalmani, G.; Rega, N.; Petersson, G. A.; Nakatsuji, H.; Hada, M.; Ehara, M.; Toyota, K.; Fukuda, R.; Hasegawa, J.; Ishida, M.; Nakajima, T.; Honda, Y.; Kitao, O.; Nakai, H.; Klene, M.; Li, X.; Knox, J. E.; Hratchian, H. P.; Cross, J. B.; Bakken, V.; Adamo, C.; Jaramillo, J.; Gomperts, R.; Stratmann, R.

E.; Yazyev, O.; Austin, A. J.; Cammi, R.; Pomelli, C.; Ochterski, J. W.; Ayala, P. Y.; Morokuma, K.; Voth, G. A.; Salvador, P.; Dannenberg, J. J.; Zakrzewski, V. G.; Dapprich, S.; Daniels, A. D.; Strain, M. C.; Farkas, O.; Malick, D. K.; Rabuck, A. D.; Raghavachari, K.; Foresman, J. B.; Ortiz, J. V.; Cui, Q.; Baboul, A. G.; Clifford, S.; Cioslowski, J.; Stefanov, B. B.; Liu, G.; Liashenko, A.; Piskorz, P.; Komaromi, I.; Martin, R. L.; Fox, D. J.; Keith, T.; Al-Laham, M. A.; Peng, C. Y.; Nanayakkara, A.; Challacombe, M.; Gill, P. M. W.; Johnson, B.; Chen, W.; Wong, M. W.; Gonzalez, C.; Pople, J. A. *Gaussian03, Revision B.05*; Gaussian Inc., Wallingford, CT, 2003.

(81) Burke, K.; Perdew, J. P.; Wang, Y. Derivation of a Generalized Gradient Approximation: the PW91 Density Functional. In *Electronic Density Functional Theory: Recent Progress and New Directions*; Dobson, J. F., Vignale, G., Mas, M. P., Eds.; Plenum: New York, 1998.

(82) Perdew, J. P. Unified Theory of Exchange and Correlation Beyond the Local Density Approximation. In *Electronic Structure of Solids*; Ziesche, P., Eschrig, H., Eds.; Akademie: Berlin, 1991.

(83) Perdew, J. P.; Burke, K.; Wang, Y. *Phys. Rev. B: Condens. Matter Mater. Phys.* **1996**, *54*, 16533–16539.

(84) Perdew, J. P.; Burke, K.; Wang, Y. *Phys. Rev. B: Condens. Matter Mater. Phys.* **1998**, *57*, 14999–14999.

(85) Perdew, J. P.; Chevary, J. A.; Vosko, S. H.; Jackson, K. A.; Pederson, M. R.; Singh, D. J.; Fiolhais, C. *Phys. Rev. B: Condens. Matter Mater. Phys.* **1992**, *46*, 6671–6687.

(86) Perdew, J. P.; Chevary, J. A.; Vosko, S. H.; Jackson, K. A.; Pederson, M. R.; Singh, D. J.; Fiolhais, C. *Phys. Rev. B: Condens. Matter Mater. Phys.* **1993**, *48*, 4978–4978.

(87) Kuchle, W.; Dolg, M.; Stoll, H.; Preuss, H. *Mol. Phys.* **1991**, *74*, 1245–1263.

(88) Hariharan, P. C.; Pople, J. A. *Theor. Chim. Acta* **1973**, *28*, 213–222.

(89) Hehre, W. J.; Ditchfie, R.; Pople, J. A. *J. Chem. Phys.* **1972**, *56*, 2257–2261.

(90) Davidson, E. R. *Chem. Phys. Lett.* **1996**, *260*, 514–518.

(91) Woon, D. E.; Dunning, T. H. *J. Chem. Phys.* **1993**, *98*, 1358–1371.

(92) Ditchfield, R. *Mol. Phys.* **1974**, *27*, 789–807.

(93) Wolinski, K.; Sadlej, A. J. *Mol. Phys.* **1980**, *41*, 1419–1430.

(94) Junk, P. C.; Steed, J. W. *J. Organomet. Chem.* **1999**, *587*, 191–194.

(95) London, F. *J. Phys. Radium* **1937**, *8*, 397–409.

(96) McWeeny, R. *Phys. Rev.* **1962**, *126*, 1028–1034.

(97) Wolinski, K.; Hinton, J. F.; Pulay, P. *J. Am. Chem. Soc.* **1990**, *112*, 8251–8260.

(98) Ravel, B.; Newville, M. *J. Synchrotron Radiat.* **2005**, *12*, 537–541.

(99) Michalowicz, A.; Moscovici, J.; Muller-Bouvet, D.; Provost, K. *J. Phys. Conf. Series* **2009**, *190*, 012034.

(100) Ankudinov, A. L.; Ravel, B.; Rehr, J. J.; Conradson, S. D. *Phys. Rev. B: Condens. Matter Mater. Phys.* **1998**, *58*, 7565–7576.